Biorheology 38 (2001) 275–304
IOS Press

Effect of secondary flow on biological experiments in the cone-plate viscometer: Methods for estimating collision frequency, wall shear stress and inter-particle interactions in non-linear flow

Harish Shankaran and Sriram Neelamegham *
Department of Chemical Engineering, State University of New York at Buffalo, Buffalo, NY 14260, USA

Received 19 March 2001
Accepted in revised form 12 June 2001

Abstract. We present a theoretical analysis of fluid flow and particle interactions in the cone-plate viscometer under conditions typically applied in biological studies. The analysis demonstrates that at higher shear rates, besides linear primary flow in the rotational direction, prominent non-linear secondary flow causes additional fluid circulation in the radial direction. Two parameters, the cone angle and Reynolds number, characterize flow in the viscometer over all ranges of shear rate. Our results indicate that secondary flow causes positional variations in: (i) the velocity gradient, (ii) the direction and magnitude of the wall shear stress at the plate surface, (iii) inter-particle collision frequency, (iv) magnitude and periodicity of normal and shear forces applied during particle–particle interactions, and (v) inter-particle attachment times. Thus, secondary flow may significantly influence cellular aggregation, platelet activation and endothelial cell mechanotransduction measurements. Besides cone-plate viscometers, this analysis methodology can also be extended to other experimental systems with complex non-linear flows.

Keywords: Neutrophil, platelet, endothelial cell, Jeffery orbits, hydrodynamic force, contact duration, two-body hydrodynamics

1. Introduction

The nature of bulk flow induced on rotation of the cone-plate viscometer affects both the interactions of particles placed in suspension in this device, and the shear stress applied on the plate surface. Exploiting these features of flow, several researchers in the biomedical/biophysical sciences have used the cone-plate viscometer to study both cell-surface receptor function and shear induced cellular activation phenomena [10,14,18,30]. These studies have influenced our understanding of the effect of fluid rheology on neutrophil, platelet, endothelial cell and smooth muscle cell function/response.

The assumption made in biological literature, that flow is uniform and linear in the cone-plate viscometer is violated at the higher shear rates. Indeed, at low shear rates the flow in the viscometer is in one dimension. There is only a rotational velocity component, which varies linearly with distance

* Address for correspondence: Sriram Neelamegham, Department of Chemical Engineering, 906 Furnas Hall, State University of New York at Buffalo, Buffalo, NY 14260, USA. Tel.: +11 716 645 2911, ext. 2220; Fax: +1 716 645 3822; E-mail: neel@eng.buffalo.edu.

from the plate surface. This flow is termed as "primary flow". While this is valid for low shear rates, at high shear rates centrifugal forces cause an outward radial motion of the fluid near the rotating cone surface and an inward radial flow near the plate. This additional radial motion of the liquid is called "secondary flow" [21,22]. Secondary flow causes a 3-dimensional flow pattern in the viscometer.

While studies in biomedical/biophysical literature typically ignore the contribution of secondary flow in altering cellular function, this feature of fluid flow may result in the application of time-varying and/or unusually high hydrodynamic forces on cells placed in the viscometer. We examine these non-linear hydrodynamic features in the current paper, and determine the conditions under which they may be prominent. A numerical solution of the detailed primary and secondary flow in the cone-plate viscometer is obtained by solving the Navier–Stokes and vorticity transport equations including the edge effects. This analysis of flow is combined with a two-body hydrodynamic interaction model to estimate the inter-particle collision frequency, shear and normal forces, and attachment times during particle collisions in the viscometer. Our analysis predicts significant positional variations in these features within the device over the range of conditions typically observed in biological experiments. Further, it demonstrates that while shear rate alone may be a good parameter to describe flow in the viscometer at low shear, the cone angle and Reynolds number are the appropriate parameters describing the fluid hydrodynamics over all ranges of shear. We have recently shown the effect of the secondary flow phenomena described here on studies of homotypic neutrophil aggregation [23]. While the current work examines the binding between equal-sized particles subjected to non-linear shear in a cone-plate viscometer, the methodology may be extended to examine interactions between particles of different sizes, and to other shearing devices where the flow is complex and non-linear.

2. Methods

The cone-plate viscometer consists of a stationary plate placed below an inverted cone. In typical biological experiments, cells are either placed in suspension [15,18,25] or plated on the stationary plate surface [10,20,30], and shear is applied by rotation of the cone. The shear rate in these studies ranges from 0 to 10,000 /sec and the cone angle varies from $1/3$ to 2 degrees. The applied shear rate is less than $\sim$2500 s^{-1} for typical studies of neutrophil and endothelial function, and it is greater than $\sim$5000 s^{-1} in studies of shear-induced platelet activation.

Dimensional analysis of the fluid flow equations for the viscometer [13] indicates that the important parameters that regulate flow in the device are (i) the cone angle, α and (ii) the dimensionless flow Reynolds number, *Re*:

$$Re = \frac{R^2\Omega}{\nu}, \tag{1}$$

where R is the radial distance to the edge of the sample being sheared (m), Ω is the angular velocity of the cone (rad/s) and ν is the kinematic viscosity of the fluid (m^2/s). In our current analysis, α is varied from 0.009 to 0.035 radians (or $1/2^\circ$ to 2°) and *Re* ranges from 0 to 1×10^5. These parameter values lie in the range of conditions observed in the above biological experiments. The largest *Re* (10^5) corresponds to the case of a 1 ml sample being sheared in a $1/2^\circ$ viscometer at a shear rate of $\sim$8000 s^{-1}.

2.1. Flow in the cone-plate viscometer

2.1.1. Primary flow in the viscometer

The spherical coordinate system employed for the solution of flow in the viscometer is described in Fig. 1A. At low shear rates, flow in a cone-plate viscometer has only a rotational velocity component about the Z_v axis, i.e., the velocity w in the ϕ direction is the only non-zero velocity component. Velocities in the radial r direction (u), and the vertical θ direction (v) are both zero. This type of flow is termed as *primary flow*.

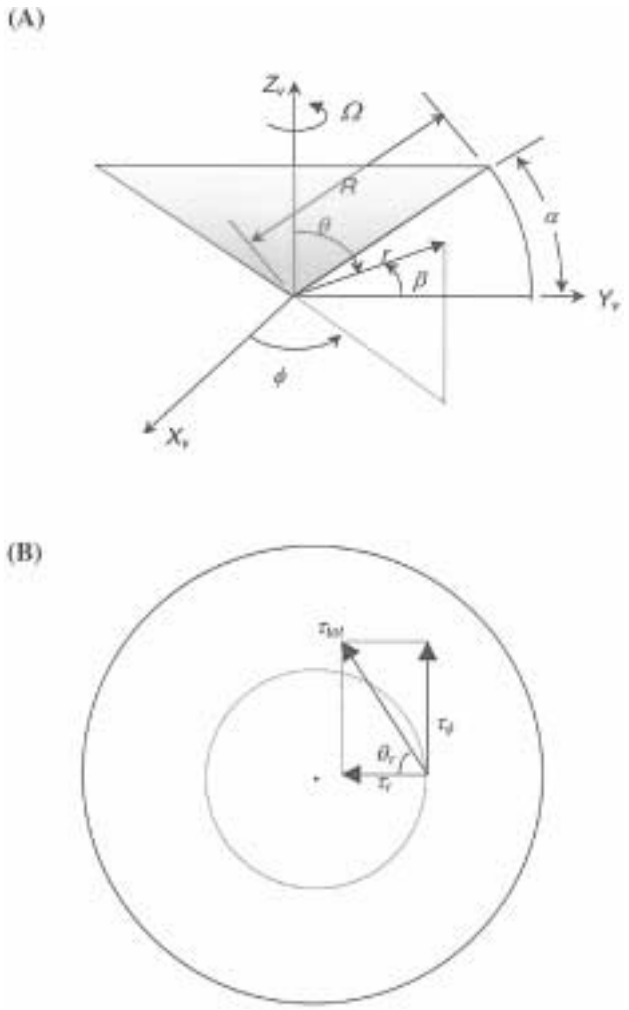

Fig. 1. (A) Coordinate system for numerical solution of flow in a cone-plate viscometer. Figure depicts schematic of a cone-plate viscometer with cone angle α and radius R. In the cartesian coordinate system Z_v coincides with the cone axis, and X_v and Y_v lie on the plate surface. The spherical coordinate system is defined by the axes (r, θ, ϕ). Ω is the angular velocity of the cone about Z_v. The angle β is defined as $\pi/2-\theta$. β varies from 0 at the plate surface to α at the cone surface. (B) Components of wall shear stress at the plate surface. τ_r is the component of wall shear stress along the radial direction r, and τ_ϕ is the component along the azimuthal direction ϕ. The total magnitude of the wall shear at the plate is $\tau_{\text{tot}}(= (\tau_\phi^2 + \tau_r^2)^{1/2})$. $\theta_\tau(=\tan^{-1}(\tau_\phi/\tau_r))$ is an angle which defines the orientation of τ_{tot} with respect to the radial direction.

During primary flow, the velocity increases linearly between the plate and the cone with increasing angle, β. The shear stress and the shear rate are uniform throughout the viscometer. For a viscometer with cone angle α being rotated with angular velocity Ω, the shear stress τ for a Newtonian fluid with viscosity μ undergoing primary flow is expressed as [7]:

$$\tau = \frac{\mu\Omega}{\tan\alpha}. \tag{2}$$

Since w is the only non-zero velocity component, the velocity gradient tensor at a radial distance r and angle β can be written in spherical coordinates as:

$$\boldsymbol{G} = \begin{bmatrix} 0 & 0 & \dfrac{\partial w}{\partial r} \\ 0 & 0 & -\dfrac{1}{r}\dfrac{\partial w}{\partial \beta} \\ -\dfrac{w}{r} & -\dfrac{w\tan\beta}{r} & 0 \end{bmatrix}. \tag{3}$$

For small cone angles, w can be expressed as ($r\Omega\cos\alpha) \cdot (\beta/\alpha)$. Here, $r\Omega\cos\alpha$ is the velocity (m/s) of fluid at the cone surface in the azimuthal direction at a radial distance r, and β/α is the dimensionless height (always < 1) of the fluid element from the plate surface. Since $\cos\alpha \approx 1$ for small cone angles, w is of the order of magnitude of $r\Omega$. Consequently, the $G_{(13)}$ and $G_{(31)}$ terms ($\partial w/\partial r$ and $-w/r$) are of the order of magnitude of Ω. The $G_{(32)}$ term ($-w\tan\beta/r$) is of the order $\Omega\alpha$. The largest term in the velocity gradient tensor is $G_{(23)}(-1/r(\partial w/\partial\beta))$ which is of the order Ω/α. If all the terms except $G_{(23)}$ are neglected, primary flow can be approximated to be a simple shear flow with a shear rate of Ω/α (s^{-1}). Ω/α is abbreviated as G, the primary flow shear rate. The approximation that flow in the cone-plate viscometer is equivalent to simple shear flow is used in most studies that examine biological phenomena.

2.1.2. Non-linear secondary flow in the viscometer

Secondary flow results when the cone angle and angular velocity of the rotating cone are increased. This additional flow occurs under conditions when significant centrifugal forces push the liquid radially out near the cone surface. The requirement of continuity causes a radial inward motion near the plate surface, thereby setting up radial fluid circulation. Thus, the velocity components (u, v and w) are all non-zero. Also, these velocity components do not vary in the azimuthal (ϕ) direction since the flow is rotationally symmetric (i.e., $\partial/\partial\phi$ terms are set to zero). The complete velocity gradient tensor $\boldsymbol{G}$ for the flow under these conditions, is written in spherical coordinates as:

$$\boldsymbol{G} = \begin{bmatrix} \dfrac{\partial u}{\partial r} & \dfrac{\partial v}{\partial r} & \dfrac{\partial w}{\partial r} \\ -\dfrac{1}{r}\dfrac{\partial u}{\partial \beta} - \dfrac{v}{r} & -\dfrac{1}{r}\dfrac{\partial v}{\partial \beta} + \dfrac{u}{r} & -\dfrac{1}{r}\dfrac{\partial w}{\partial \beta} \\ -\dfrac{w}{r} & -\dfrac{w\tan\beta}{r} & \dfrac{u}{r} + \dfrac{v\tan\beta}{r} \end{bmatrix}. \tag{4}$$

As seen, all the components of $\boldsymbol{G}$ are non-zero. Further, if the individual velocity components (u, v and w) vary non-linearly with position in the viscometer, the velocity gradient tensor may also vary with spatial coordinates.

2.1.3. Numerical solution for the flow

In this section, we describe a strategy to estimate the velocities u, v and w in the viscometer. Previously, researchers [22,29] have modeled the flow in the viscometer by developing analytical perturbation solutions of the Navier–Stokes and continuity equations. However, these approximate solutions of flow are limited to low *Re* (*Re* $<\sim$7000 for a 2° cone), and usually do not account for the edge effects due to the finite sample volume in the viscometer. To overcome these limitations we chose to use the approach of Fewell and Hellums [13], who developed an exact numerical solution for the flow by solving the dimensionless vorticity transport equation and Navier–Stokes equation (relevant equations from [12,13] are listed in Appendix A). In modeling the flow in the viscometer, the free surface at the edge of the sample volume is assumed to be spherical. The no-slip boundary condition is applied at both the cone and the plate surfaces. In addition, the sheared sample is assumed to be a Newtonian fluid, as is typically the case when dilute cell suspensions are sheared in biological experiments.

We obtained a numerical solution of the governing equations (Appendix A) using a finite difference scheme for the space derivatives. The "exponentially stretched" grid employed in spherical coordinates for the finite difference analysis is described in Fig. 2 of [13]. It consists of N grid points in the θ direction, and M grid points in the radial (r) direction. On transforming the space derivatives in the governing equations and boundary conditions to the finite difference grid, the resulting ordinary differential equations (ODEs) in the time variable could be solved for the velocity field in the device (see [12] for details).

Our treatment of this system of ODEs differs from that of the previous work [13] in one important respect. Fewell et al. in their analysis treated the ODEs as linear algebraic equations, and employed an alternating direction implicit method for the solution. They had to perform inner iterations at each time step to ensure convergence of the non-linear terms. By restricting the maximum number of iterations performed to a fixed small number, the authors could achieve convergent steady state solutions, although at each intermediate time step, the true transient solution was not obtained. In our current analysis, however, no attempt was made to linearize the system of ODEs. The system of differential–algebraic equations in time, obtained by discretizing the space derivatives was solved exactly at each time step using the Petzold–Gear BDF method [8]. Thus, in addition to the steady state solution, true transient solutions were also obtained. This enabled us to determine the actual time taken for the flow in the viscometer to reach steady state. A solution was defined as having reached steady state when the maximum fractional variation in one of the dependent variables, the covariant component of the rotational velocity Γ ($= rw\cos\beta$), between time steps was less than a preset value of 10^{-8}. Using this approach, we computed the steady state velocity profiles (u, v, w) and the stream function (ψ) over a range of Reynolds numbers and cone angles. The steady-state flow solution was then used to calculate the velocity gradient tensor $\boldsymbol{G}$ using Eq. (4). All subsequent calculations in this paper are performed with the velocity gradient tensor obtained using the steady-state flow solution.

2.2. Computation of wall shear stress

Once the steady-state velocity gradient was obtained as described above, we computed the effect of secondary flow on the wall shear stress at the plate surface. The velocity gradient $\boldsymbol{G}$ for flow can be

broken up into the rate-of-strain tensor $\boldsymbol{S}$ and the vorticity tensor $\boldsymbol{\Lambda}$, which represent the extensional and rotational components of the local flow field according to the equation [3]:

$$\boldsymbol{G} = \boldsymbol{S} + \boldsymbol{\Lambda}. \tag{5}$$

The rate of strain tensor $\boldsymbol{S}$ for the flow is expressed as $\boldsymbol{S} = 1/2(\boldsymbol{G} + \boldsymbol{G}^T)$ and the vorticity tensor $\boldsymbol{\Lambda}$ as $\boldsymbol{\Lambda} = 1/2(\boldsymbol{G} - \boldsymbol{G}^T)$, where $\boldsymbol{G}^T$ is the transpose of $\boldsymbol{G}$. The tensor $\boldsymbol{S}$ defined in this fashion is symmetric, while $\boldsymbol{\Lambda}$ is anti-symmetric. The elements of the tensor $\boldsymbol{S}$ evaluated at the plate surface provide information on the wall shear stress. The wall shear stress in the azimuthal and radial directions can be expressed as $\tau_\phi = 2\mu S_{(32)}$ and $\tau_r = 2\mu S_{(13)}$. These components of the wall shear stress are depicted schematically in Fig. 1B. The total shear stress at the wall is $\tau_{\text{tot}} = (\tau_r^2 + \tau_\phi^2)^{1/2}$. The orientation of the shear stress at the wall θ_τ with respect to the radial component, depends on the relative magnitudes of the shear stress components and is defined as $\theta_\tau = \tan^{-1}(\tau_r/\tau_\phi)$. The numerically computed velocity gradient was employed to calculate the magnitude and the orientation of the wall shear stress at various radial positions on the plate surface.

2.3. Inter-particle collision frequency

When a cell suspension is subjected to shear in a cone-plate viscometer, the rate of aggregation depends upon (i) the inter-particle collision frequency and (ii) the probability of the collisions resulting in stable aggregate formation. In this section, we present a methodology to calculate the inter-particle/cellular collision frequency (number of collisions/m^3/s) in a fluid subjected to non-linear flow.

Collision frequency is a function of the local fluid velocity gradient, cell concentration and cell size. In our current analysis, we assume that the sheared fluid consists of a suspension of spherical particles with effective radius r_{eff}. r_{eff} includes the cell radius and protrusions on the surface such as surface microvilli. The concentration of these cells/particles, denoted N_P, is assumed to be constant throughout the viscometer. In the analysis, inter-particle collision frequencies are calculated by assuming that cells follow linear trajectories, and are not affected by the presence of the lubrication layer surrounding the colliding species. When such particles collide, it is possible to imagine a spherical surface with radius $2r_{\text{eff}}$ centered around one of the spheres (Fig. 2). This imaginary spherical surface is called the *collision sphere*. It is seen that if the center of any other particle/cell passes through this collision sphere, collision between the particles/cells will occur. During simple shear, the velocity gradient tensor has only one non-zero component, the shear rate $G(= G_{(23)})$. The collision frequency under these conditions is given by Smoluchowski's equation [6,11,24]:

$$\text{Collision frequency} = \frac{16}{3} G N_P^2 r_{\text{eff}}^3. \tag{6}$$

The calculation of collision frequency under secondary flow conditions in the cone-plate viscometer is more complex. Here, the velocity gradient tensor has multiple non-zero components. In such cases, the contribution to collision frequency from each of the components needs to be calculated and combined in an appropriate fashion to obtain the overall collision frequency.

We present here an approach to calculate collision frequency by estimating the total mass transfer rate of particles/cells into the collision sphere. In the space-fixed coordinate system (Fig. 2), X_1, X_2 and X_3 coincide locally with the r, θ and ϕ directions of the viscometer. Consider now an area element dA on the surface of the collision sphere (Fig. 2). The polar and azimuthal angles θ_1 and ϕ_1 with reference to

axis X_1 describe the location of this element, and $\boldsymbol{n}$ is a unit normal vector directed out of this element. $\boldsymbol{u}_c$ is the relative velocity between the centers of the colliding spheres. The total mass transfer rate across the surface of the collision sphere can be written as:

$$C_P = -\int_{\text{collision sphere}}\int N_P \;\; \boldsymbol{n}\cdot\boldsymbol{u}_c \,\mathrm{d}A. \tag{7}$$

The negative sign in the right hand side accounts for the direction of mass transfer. Thus, mass transfer into the sphere results in a positive C_P value and vice versa. From the spherical coordinates system in Fig. 2, we can express the differential area (dA) and outward normal vector ($\boldsymbol{n}$) as functions of θ_1 and ϕ_1:

$$\mathrm{d}A = [2r_{\text{eff}}]^2 \sin\theta_1 \mathrm{d}\theta_1 \mathrm{d}\phi_1, \tag{8}$$

$$\boldsymbol{n} = (\cos\theta_1 \quad \sin\theta_1\cos\phi_1 \quad \sin\theta_1\sin\phi_1). \tag{9}$$

The relative velocity vector $\boldsymbol{u}_c$ can be written as [3]:

$$\boldsymbol{u}_c = \boldsymbol{r}_c \cdot \boldsymbol{G}. \tag{10}$$

Here, $\boldsymbol{G}$ is the local velocity gradient tensor (Eq. (4)) and $\boldsymbol{r}_c$ is the position vector of the area element on the collision sphere which can be expressed as:

$$\boldsymbol{r}_c = 2r_{\text{eff}}(\cos\theta_1 \quad \sin\theta_1\cos\phi_1 \quad \sin\theta_1\sin\phi_1). \tag{11}$$

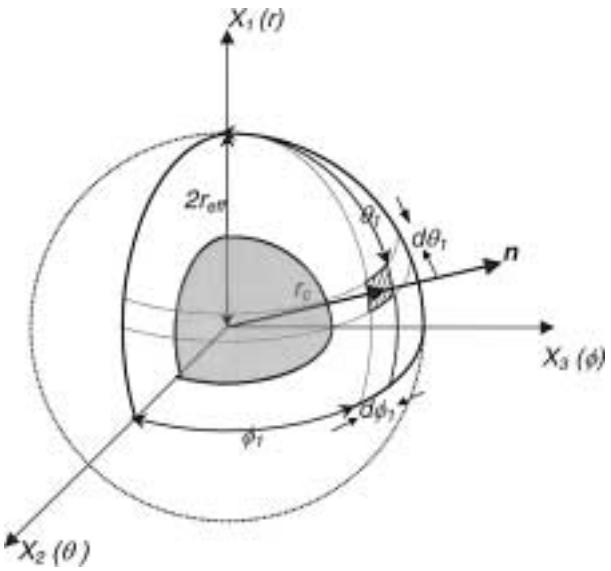

Fig. 2. Coordinate system for collision frequency calculations. The frequency of collision of the shaded (gray) inner sphere of radius r_{eff} placed at the center of the cartesian space-fixed coordinate system is calculated. The outer sphere with radius $2r_{\text{eff}}$ depicted by dotted lines represents the collision sphere. If the center of any particle enters the collision sphere, collision between this particle and the gray sphere occurs. Calculations are performed for the differential area element depicted as the shaded region on the surface of the collision sphere. The position of this area element is defined by the polar angle θ_1, the azimuthal angle ϕ_1, and the position vector $\boldsymbol{r}_c$. The size of the element is defined by the angles $\mathrm{d}\theta_1$ and $\mathrm{d}\phi_1$. $\boldsymbol{n}$ is the unit normal vector to this element pointing in a direction radially outward from the surface of the collision sphere.

To evaluate the double integral (Eq. (7)) over the entire surface of the collision sphere, the collision sphere was divided into a series of discrete area elements by varying θ_1 from 0 to π, and ϕ_1 from 0 to 2π in discrete steps to account for all possible collision orientations. θ_1 and ϕ_1 were discretized into N_θ and N_ϕ elements respectively according to:

$$\theta_{1k} = (k-1)\pi/(N_\theta - 1), \quad k = 1, 2, \ldots, N_\theta, \tag{12a}$$

$$\phi_{1l} = (l-1)2\pi/(N_\phi - 1), \quad l = 1, 2, \ldots, N_\phi. \tag{12b}$$

For each of the differential area elements $\mathrm{d}A$ located at position (θ_{1k}, ϕ_{1l}), the mass transfer rate into the element was evaluated by accounting for all the nine components of the velocity gradient tensor, $G_{(ji)}$. This can be expressed algebraically as:

$$\mathrm{d}C_P(\theta_{1k}, \phi_{1l}) = -N_P\,\mathrm{d}A(\theta_{1k}, \phi_{l1}) \sum_{i=1}^{3} \left\{ n_{(i)}(\theta_{1k}, \phi_{1l}) \sum_{j=1}^{3} \left[r_{c_{(j)}}(\theta_{1k}, \phi_{1l}) G_{(ji)} \right] \right\}. \tag{13}$$

A positive value of $\mathrm{d}C_P$ for the area element implies mass transfer into the collision sphere. Particle/cell collision thus takes place in this element. A negative value of $\mathrm{d}C_P$ implies mass transfer away from the collision sphere and the absence of collisions in this element. Besides providing collision frequency statistics, the above equation is also used to generate the weighting functions to estimate the orientation of colliding particles in the viscometer as detailed later. The overall collision frequency for secondary flow was obtained by summation of positive $\mathrm{d}C_P$ values over all possible collision orientations according to:

$$C_P = \sum_{k=1}^{N_\theta} \sum_{l=1}^{N_\phi} \mathrm{d}C_P^{\#}(\theta_{1k}, \phi_{1l}), \quad \text{where } \mathrm{d}C_P^{\#} = \begin{cases} \mathrm{d}C_P & \text{if } \mathrm{d}C_P > 0, \\ 0 & \text{if } \mathrm{d}C_P \leqslant 0. \end{cases} \tag{14}$$

It should be noted that C_P equals the number of collisions per particle, and not the collision frequency per unit volume. The collision frequency $C(r_i^*, \beta_j)$ per unit volume evaluated at the (i, j)th finite-difference node in the viscometer, can be obtained by multiplying C_P with $N_P/2$, and can be expressed as:

$$C(r_i^*, \beta_j) = \frac{N_P}{2} C_P. \tag{15}$$

The factor of $1/2$ is introduced to prevent double counting of particles/cells.

The collision frequency obtained above is a local value evaluated using the local flow gradient $\boldsymbol{G}$. In our simulations, we employed the numerically computed flow gradients (Eq. (4)) to calculate the collision frequency at each of the grid points in the viscometer. A volume-averaged collision frequency, $\overline{C}$ for the entire viscometer was then computed using the expression:

$$\overline{C} = \frac{\sum_{i=1}^{M} \sum_{j=1}^{N} C(r_i^*, \beta_j) \Delta V(r_i^*, \beta_j)}{\sum_{i=1}^{M} \sum_{j=1}^{N} \Delta V(r_i^*, \beta_j)}, \tag{16}$$

where $\Delta V(r_i^*, \beta_j)$ is volume of the element centered around the node (i, j).

2.4. Doublet interactions

In cellular aggregation experiments performed in the cone-plate viscometer, the probability of inter-cellular collisions resulting in stable aggregate formation is dependent on the nature of fluid flow. Specifically, the inter-cellular force and the attachment time are important hydrodynamic parameters, which determine the fate of a transient aggregate formed following collision. The inter-particle normal force acts along the line joining the centers of the interacting particles; while compressive normal forces push the cells towards each other, tensile forces tend to break up the aggregate. Once a doublet is formed, it is subjected to successive cycles of compressive and tensile normal force. The attachment time is defined as the time the doublet spends in the compressive force zone following cell–cell collision. The detailed derivation of the equations for the inter-particle normal force and particle trajectory is provided in Appendix B based on work by [4,9]. In this section, we present the final equations and describe the strategy employed to evaluate the effect of secondary flow on the normal force and the attachment time. Although the calculations are performed for the case of secondary flow in the cone-plate viscometer, the scheme presented here can be extended to any flow field as long as the velocity gradient $\boldsymbol{G}$ is known.

2.4.1. Assumptions

In our analysis, two-body hydrodynamic calculations are performed for spheres with some surface roughness. Here, we assume that the particles are "neutrophil-like" with a radius (r_P) of 3.7 μm and surface microvilli of length 0.4 μm (λ) [23]. Thus, in our calculations of inter-particle forces and attachment times, we treat the particles as equal-sized spheres of radius 3.7 μm with a closest separation distance between spheres of 0.8 μm. This analysis can be extended to heterotypic particle interactions as discussed elsewhere [4,9].

Several modeling assumptions are made here regarding the nature of particle interactions. First, following inter-particle collision, particle doublets are assumed to behave like rigid dumbbells. Similar experimental observations of rigid dumbbell formation, following the collision of blood cells have been made earlier [27]. If slip between the interacting spheres occurs in the experimental system considered, the analysis presented here would not be strictly valid and parts of the calculation would have to be appropriately modified. Second, while calculating inter-particle interactions, the doublet is assumed to be subjected to a time-invariant velocity gradient, which depends on the coordinates in the viscometer where particle collision occurs. This is in spite of the positional variations in the velocity gradient tensor within the viscometer. This assumption appears to be reasonable since, over the range of *Re* values and cone angles tested, the time-period of doublet rotation is $\sim$2–3 orders of magnitude smaller than the time scale of fluid re-circulation induced by secondary flow. Therefore, the doublet undergoes several rotations during the time taken for it to translate from the point of collision to an area with a significantly different velocity gradient. Third, inertial effects [17] are neglected in the particle hydrodynamic analysis. As shown elsewhere [1] this feature does not significantly affect particle trajectories over the first few rotations under our simulation conditions. Finally, in our analysis, it is assumed that although secondary flow results in a non-linear flow field, the flow is approximately linear in the length scales of the sphere diameter where the two colliding species interact. Given the size of the interacting particles, this is a reasonable assumption.

2.4.2. Inter-particle force for a rigid dumbbell

For a rigid dumbbell suspended in a locally linear flow with velocity gradient $\boldsymbol{G}$, the inter-particle normal force can be written as (see Appendix B for derivation):

$$F'_{(3)} = -\mu\left(-\frac{1}{2}br_D + f + g\right)\boldsymbol{O}_F : \boldsymbol{G}, \tag{17}$$

where μ is the fluid viscosity, b, f and g are force-torque coefficients for a doublet of equal-sized particles, which are tabulated in [4] as functions of the size of the interacting particles and the separation distance between them, $r_D[= 2(r_P + \lambda)]$ is the size of the rigid dumbbell, $\boldsymbol{G}$ is the velocity gradient tensor (Eq. (4)) and $\boldsymbol{O}_F$ is a tensor which can be written in terms of the orientation of the doublet (θ_1, ϕ_1) (see Fig. 8, Appendix B) as

$$\boldsymbol{O}_F = \begin{pmatrix} \cos^2\theta_1 & \frac{1}{2}\sin 2\theta_1 \cos\phi_1 & \frac{1}{2}\sin 2\theta_1 \sin\phi_1 \\ \frac{1}{2}\sin 2\theta_1 \cos\phi_1 & \sin^2\theta_1 \cos^2\phi_1 & \frac{1}{2}\sin^2\theta_1 \sin 2\phi_1 \\ \frac{1}{2}\sin 2\theta_1 \sin\phi_1 & \frac{1}{2}\sin^2\theta_1 \sin 2\phi_1 & \sin^2\theta_1 \sin^2\phi_1 \end{pmatrix}. \tag{18}$$

In our analysis of the normal force experienced by rigid dumbbells, we calculated $F'_{(3)}$ for all possible doublet orientations ($0 \leqslant \theta_1 \leqslant \pi$, and $0 \leqslant \phi_1 \leqslant 2\pi$) at the different grid points in the viscometer using the numerically computed values of the local flow gradient $\boldsymbol{G}$. For each (i, j)th node, we determined the maximum normal force, $F_{\max}(r_i^*, \beta_j)$ using the definition:

$$F_{\max}(r_i^*, \beta_j) = \mathrm{Max}\left[F'_{(3)}(\theta_1, \phi_1)\right]; \quad 0 \leqslant \theta_1 \leqslant \pi;\ 0 \leqslant \phi_1 \leqslant 2\pi. \tag{19}$$

$F_{\max}(r_i^*, \beta_j)$ is a local parameter that depends on position in the device. These $F_{\max}(r_i^*, \beta_j)$ values were weighted by the number of inter-particle collisions at each grid point, and averaged to obtain the collision-averaged maximum normal force, $\bar{F}_{\max}$ for the entire viscometer using the expression:

$$\bar{F}_{\max} = \frac{\sum_{i=1}^{M}\sum_{j=1}^{N} F_{\max}(r_i^*, \beta_j) C(r_i^*, \beta_j) \Delta V(r_i^*, \beta_j)}{\sum_{i=1}^{M}\sum_{j=1}^{N} C(r_i^*, \beta_j) \Delta V(r_i^*, \beta_j)}. \tag{20}$$

Therefore, a rigid particle doublet in a viscometer, formed upon inter-particle collision, would on an average experience a maximum breakup force of $\bar{F}_{\max}$.

We note that these calculations of local and global maximum force (Eqs (19), (20)) do not account for the distribution of collisions that occur at each position. Over time, not all doublet orientations ($0 \leqslant \theta_1 \leqslant \pi$ and $0 \leqslant \phi_1 \leqslant 2\pi$) are achieved with equal probability. Further, glancing collisions are more frequent than head-on collisions, and the former may not experience the peak force $F_{\max}(r_i^*, \beta_j)$. Such considerations are important in the context of cellular aggregation studies where there is a competition between the rate of inter-cellular bond formation following particle collision and the applied hydrodynamic forces that act to stress/break these bonds. Here, the efficiency with which stable aggregates are formed following particle collision is a strong function of collision orientation. For such calculations, individual collision orientations will have to be accounted for and the fate of the particles would have to be followed with time. The methodology for such calculations is detailed in another paper [23], where we follow the fate of individual neutrophil-neutrophil aggregates with time following collision.

2.4.3. Rotation of a rigid dumbbell and calculation of inter-particle attachment time

The attachment time is defined as the time the doublet formed upon cell–cell collision spends in the compressive force regime prior to experiencing a tensile force. It depends on the initial orientation of the colliding species. In our calculations, the initial collision orientation was computed based on the collision frequency function (Eq. (13)), since this equation quantifies the number of collisions ($\mathrm{d}C_P$) for a given collision orientation (θ_1, ϕ_1) of the area element ($\mathrm{d}A$) on the collision sphere. Normalization of $\mathrm{d}C_P$ with the local collision frequency, $C(r_i^*, \beta_j)$ (Eq. (15)), yielded a distribution function that described the variation in the frequency of collision with particle collision orientation. In our computations, this distribution function was generated for each node in the viscometer. Based on the distribution function, we then generated a similar pattern of weighted random numbers using an IMSL$^{\mathrm{TM}}$ (Visual numerics Inc., Houston, TX) routine *RNGCS* [2]. These random numbers were then used to obtain N_{col} number of collision orientations at each node point in the viscometer. Thus, the collision orientations considered in this manuscript account for the pattern of cell–cell collisions that occur as a result of secondary flow. Each of these initial collision orientations was denoted as $(\theta_1^0, \phi_1^0)_k$, where k varies from 1 to N_{col}.

Calculation of the attachment time requires solution of the equations describing the rotation of the rigid dumbbell. The rotational trajectory of the rigid dumbbell formed following collision can be expressed by the following equations (see Appendix B for derivation):

$$\frac{\mathrm{d}\theta_1}{\mathrm{d}t} = \boldsymbol{O}_\theta : \boldsymbol{G}, \tag{21}$$

$$\frac{\mathrm{d}\phi_1}{\mathrm{d}t} = \boldsymbol{O}_\phi : \boldsymbol{G}, \tag{22}$$

where $\boldsymbol{G}$ is the velocity gradient tensor (Eq. (4)) and $\boldsymbol{O}_\theta$, $\boldsymbol{O}_\phi$ are tensors given by the equations:

$$\boldsymbol{O}_\theta = \frac{1}{2}\begin{pmatrix} \nu_D \sin 2\theta_1 & (1-\nu_D\cos 2\theta_1)\cos\phi_1 & (1-\nu_D\cos 2\theta_1)\sin\phi_1 \\ -(1+\nu_D\cos 2\theta_1)\cos\phi_1 & -\nu_D \sin 2\theta_1 \cos^2\phi_1 & -\frac{1}{2}\nu_D \sin 2\theta_1 \sin 2\phi_1 \\ -(1+\nu_D\cos 2\theta_1)\sin\phi_1 & -\frac{1}{2}\nu_D \sin 2\theta_1 \sin 2\phi_1 & -\nu_D \sin 2\theta_1 \sin^2\phi_1 \end{pmatrix}, \tag{23}$$

$$\boldsymbol{O}_\phi = \frac{1}{2}\begin{pmatrix} 0 & (\nu_D-1)\cot\theta_1 \sin\phi_1 & -(\nu_D-1)\cot\theta_1\cos\phi_1 \\ (\nu_D+1)\cot\theta_1 \sin\phi_1 & \nu_D \sin 2\phi_1 & (1-\nu_D\cos 2\phi_1) \\ -(\nu_D+1)\cot\theta_1\cos\phi_1 & -(1+\nu_D\cos 2\phi_1) & -\nu_D \sin 2\phi_1 \end{pmatrix}. \tag{24}$$

The quantity ν_D in Eqs (23), (24) is the (flow-independent) angular velocity coefficient of the rigid dumbbell, which is given in Eq. (B.11) of Appendix B in terms of the force-torque coefficients for the dumbbell.

In order to estimate the attachment time t^a for a specific collision orientation defined by $(\theta_1^0, \phi_1^0)_k$, Eqs (21) and (22) were solved for the trajectory of the rotating dumbbell using the Petzold–Gear BDF method [8] with the initial conditions $(\theta_1, \phi_1) = (\theta_1^0, \phi_1^0)_k$. The inter-particle normal force $F'_{(3)}$ was simultaneously calculated at each time step using Eq. (17). The solution was continued until a positive value of $F'_{(3)}$ was obtained, and by definition the time taken to meet this condition was equal to the attachment time t^a.

At each (i, j)th node in the viscometer, we also estimated the average attachment time $t^a_{\text{avg}}(r^*_i, \beta_j)$. This was estimated by averaging t^a over all N_{col} initial collision orientations at that point according to:

$$t^a_{\text{avg}}(r^*_i, \beta_j) = \frac{\sum_{k=1}^{N_{\text{col}}} t^a(\theta^0_1, \phi^0_1)_k}{N_{\text{col}}}. \tag{25}$$

In our analysis, we typically averaged over 1000 collisions (i.e., $N_{\text{col}} = 1000$). The local t^a_{avg} values obtained above were further averaged over the entire volume of the viscometer to yield the collision-averaged attachment time $\bar{t}^a_{\text{avg}}$using the expression:

$$\bar{t}^a_{\text{avg}} = \frac{\sum_{i=1}^{M}\sum_{j=1}^{N} t^a_{\text{avg}}(r^*_i, \beta_j) C(r^*_i, \beta_j) \Delta V(r^*_i, \beta_j)}{\sum_{i=1}^{M}\sum_{j=1}^{N} C(r^*_i, \beta_j) \Delta V(r^*_i, \beta_j)}. \tag{26}$$

3. Results and discussion

3.1. Time-taken for the flow to reach steady state

A numerical solution for the flow was obtained by solving the governing equations. In comparison to the alternating direction implicit method [13], our approach which utilized the Petzold–Gear BDF method resulted in considerable savings in computation time. Simulations performed on a 500 MHz PC typically required less than 2 minutes of CPU time to achieve steady state. In our calculations, a mesh with 11 grid points in the radial direction (i.e, $M = 11$) and 15 grid points in the θ direction (i.e., $N = 15$) was employed. The choice of M and N were based on our observation that increasing the resolution of the grid any further resulted in a substantial increase in computation time without markedly changing the results. For example, the computation time increased 15 fold for a grid with $M = 13$ and $N = 21$, but the solution as determined by the computed maximum stream function value changed by less than 3%.

Times needed for flow in the viscometer to reach steady state are given in Table 1. As seen, for a cone angle of 2°, increasing Reynolds number from 1×10^4 to 3×10^4 caused a ∼3 fold increase in time to reach steady state (from 0.063 to 0.192 seconds). Over the range of conditions tested, the time taken to reach steady state increased approximately linearly with Reynolds number. Overall, our results indicate that the transient nature of the flow is apparent only within the first second of the application of shear. Therefore the flow features in biological assays, where the earliest sampling is done at ∼10 s [19,25], corresponds to steady-state conditions.

Table 1
Time taken for the flow in a 2° cone-plate viscometer at $G = 1500\ \text{s}^{-1}$ to reach steady state

Reynolds number	Time (s)
1×10^2	5.35×10^{-4}
8×10^2	4.20×10^{-3}
5×10^3	3.06×10^{-2}
1×10^4	6.30×10^{-2}
3×10^4	1.92×10^{-1}

3.2. Steady-state velocity profile: Secondary flow increases with cone angle and Reynolds number

The numerical solution methodology was employed to obtain steady-state flow profiles as described in Methods. The steady-state solution is identical to that of Fewell and Hellums [12,13]. Figure 3A illustrates the steady-state velocity profiles for both primary and secondary flow at a dimensionless radial position of 0.832 from the cone apex, for fluid being sheared at $Re = 3 \times 10^4$ in a 2° cone-plate viscometer. The results are expressed in dimensionless form where the velocity components are given by $u^* = u/R\Omega$, $v^* = v/R\Omega$, $w^* = w/R\Omega$ and the radial distance r is normalized using the sample radius to yield $r^*(r^* = r/R)$. In the case of primary flow, the fluid velocity only has a rotational component (w_p^*), which increases linearly with angular position β. Secondary flow, however, caused a non-linear change in rotational velocity (w^*) with β. In addition, the radial (u^*) and vertical (v^*) velocity components under secondary flow were also non-zero. In the radial direction, flow near the cone surface moved out towards the periphery of viscometer, while it moved back towards the cone apex near the plate surface. This reversal in the direction of flow was manifested in the form of changes in the sign of u^* at $\beta = 0.019$ radians.

We examined the changes in the contribution of secondary flow with radial position, by calculating the dimensionless rotational velocity, w^* under the above mentioned flow conditions (Fig. 3B). As illustrated, while w^* increased approximately linearly with angular position β in the inner half of the cone (i.e., for $r^* < 0.5$), it became increasingly non-linear near the periphery of the device. Near the edge of the sample (say $r^* = 0.98$), the rotational velocity increased more rapidly near the plate surface (for $\beta < 0.007$) in comparison to regions near the rotating cone. Three distinct regions were apparent: (i) a region of steep increase in velocity near the plate surface ($\beta < 0.007$), (ii) a plateau region ($0.007 < \beta < 0.025$) where the velocity gradient was close to zero, and (iii) a region near the cone surface ($\beta > 0.025$) where the velocity gradient was high but far less than that near the plate surface. These observations suggest that the non-linear nature of the fluid flow increases with radial distance away from the vertex of the cone. The dramatic variations in velocity profile near the edge, including the high gradients near the plate surface, are due to the enhanced fluid motion in the vertical direction which causes a substantial downward motion of fluid towards the plate thereby enhancing the rotational flow near the plate.

Overall, centrifugal forces push the liquid radially outward near the cone surface and the requirement of continuity causes an inward flow at the plate surface, thereby setting up fluid circulation (Fig. 3C). Here, the streamlines of fluid motion are illustrated as a contour plot of the stream function, ψ^*. The magnitude of the stream function seen here is a measure of the volumetric flow rate of fluid circulation in the r–θ plane, which in turn is a measure of the extent of secondary flow. The maximum stream function, $\psi^*_{\max}$, in this figure is 8×10^{-4}. Note that in this figure and in the grayscale panels that follow, in order to simplify the presentation, we have converted the curvilinear grid coordinates (r^*, β) to cartesian coordinates. For small cone angles, in cartesian coordinates, the radial distance on the plate surface (X coordinate) $= r^* \cos\beta \approx r^*$. Similarly the vertical distance from the plate surface (Y coordinate) $= r^* \sin\beta \approx r^*\beta$. These conversions were performed for each of the $M \times N$ grid points in the viscometer. The spherical nature of the free surface is not readily apparent here, since the cone angle is small.

Next, we examined the effect of varying *Re* and α, on the extent of secondary flow in the viscometer (Fig. 3D). In this figure, the maximum value of the stream function $\psi^*_{\max}$ is presented over a range of Reynolds numbers and cone angles. The top X-axis also depicts the conversion from Reynolds number to shear rate for each cone angle Eq. (1) (assuming $R = 25$ mm). In all the simulations, the maximum stream function occurred at an N value of 8 (halfway between the cone and the plate surface), and M values varying between 4 and 6 which correspond to points near the edge of the viscometer. At low

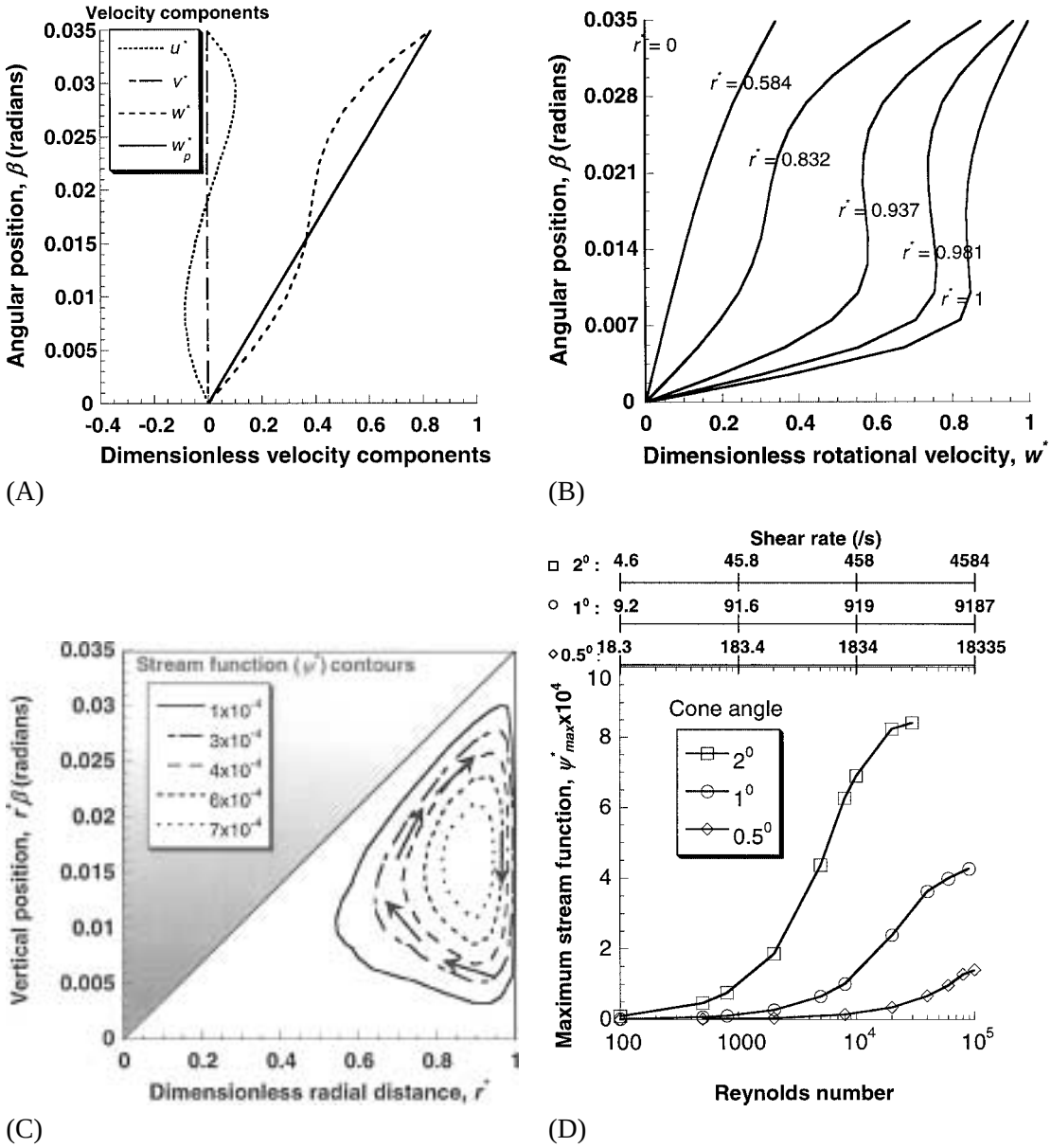

Fig. 3. Velocity profiles in the cone-plate viscometer due to secondary flow. The governing equations for the flow were solved using a finite difference scheme to obtain the flow field in the viscometer. (A) Variation of fluid velocity components with distance from the plate surface at a dimensionless radial distance (r^*) of 0.832 and Reynolds number (*Re*) of 3×10^4 for a cone angle (α) of 2°.u^*, v^* and w^* are the dimensionless velocity components in the r, θ, and ϕ directions respectively. w_p^* is the primary flow velocity which is solely in the ϕ direction. (B) Variation of the rotational velocity component w^* with position in the viscometer for $\alpha = 2^\circ$ at $Re = 3 \times 10^4$. (C) Contour plot with streamlines of the flow between the cone and plate surfaces at $Re = 3 \times 10^4$ for a 2° cone. Here, the curvilinear grid coordinates (r^*, β) were converted to cartesian coordinates according to: X coordinate $= r^*; Y$ coordinate $= r^*\beta$. Contour lines depict lines with equal stream function, ψ^*. Arrows indicate direction of fluid flow. Shaded upper-left region of the plot represents the cone surface. (D) Variation of $\psi^*_{\max}$, the dimensionless maximum stream function in the viscometer with *Re* and α. The shear rate corresponding to each *Re* is indicated on the top of panel D for the three different cone angles. The transformation from *Re* to shear rate is performed while assuming a fixed sample radius $R = 25$ mm.

Reynolds numbers, the position of $\psi^*_{\max}$ was closer to the edge ($M = 4$), and it moved radially inward ($M > 4$) with increasing Reynolds number (results not shown). Increasing both the Reynolds number and cone angle, resulted in an increase in the magnitude of $\psi^*_{\max}$.

This analysis when coupled with the dimensional analysis of the flow equations [13], indicates that the flow parameters which determine the extent of secondary flow in the cone-plate viscometer are: (i) the flow Reynolds number ($Re = R^2\Omega/\nu$), and (ii) the cone angle, α. In the context of biological experiments secondary flow may cause positional variations in the velocity gradient above a *Re* of ∼1000. Such conditions are encountered in most biological experiments that study platelet, neutrophil or endothelial cell function. Also since Re is a function of sample radius R, changing sample volume in experiments with the same angular velocity may alter the flow patterns in the viscometer.

3.3. The magnitude and orientation of wall shear stress varies with position on the plate surface

For primary flow, the wall shear stress does not vary with radial position. It can be expressed as $\tau = \mu G$, where μ is the fluid viscosity and G ($= \Omega/\alpha$) is the applied shear rate. This shear stress acts along the direction of cone rotation (i.e., the ϕ direction) and therefore θ_τ is always 90°, independent of position on the plate surface. Secondary flow however altered both the magnitude and direction of the shear stress at the plate by introducing a non-zero radial component of shear force (Fig. 4). Consequently, the net force did not act along the direction of rotation (Fig. 4A). While the shear stresses at both the edge and vertex of the viscometer were aligned in the azimuthal direction, the orientation (θ_τ) with respect to the radial direction decreased at intermediate radial distances (r^*) of ∼0.5–0.9. Our results indicate that for a cone angle of 2° and *Re* ranging from 8×10^3 to 3×10^4, θ_τ may lie in the range from ∼65° to 50°.

In addition to alterations in the orientation of the wall shear stress, secondary flow also caused an increase in the magnitude of the shear stress with radial position away from the cone vertex (Fig. 4B). A sharp increase in shear stress was observed at the outer edge of the viscometer over the entire range of flow conditions tested. This is consistent with our observation of increased flow gradients near the plate surface at the edge of the viscometer. At $Re = 3\times10^4$ for a 2° cone, the magnitude of shear forces applied at the periphery of the viscometer was ∼ 6 fold that predicted by primary flow analysis. Increasing cone angle and *Re* augmented the extent of wall shear stress applied on the plate surface (Fig. 4C).

Based on these observations, we conclude that secondary flow may augment the applied wall shear stress at the outer edge of the viscometer in the range of biological/biophysical experiments. Previous studies of endothelial cell response to shear have been conducted in cone-plate viscometers at apparent wall shear stresses of ∼2 Pa [10,28]. Under these conditions, our analysis predicts a ∼5 fold increase in wall shear stress at the edge of the viscometer compared to that predicted by primary flow analysis. Thus in these experiments, some cells may experience shear stresses of up to ∼10 Pa. Ignoring secondary flow effects in these experiments could lead to incorrect conclusions regarding the range of shear stresses required for endothelial cell mechanotransduction.

3.4. Local collision frequency is a function of Re and α

In the case of primary flow, the collision frequency can be computed based on Smoluchowski's two-body collision theory (Eq. (6)). This analysis predicts a constant collision frequency throughout the viscometer. The secondary flow velocity gradient $\boldsymbol{G}$, on the other hand varies with position in the viscometer. Consequently, in this case, the collision frequency also varied with position in the device (Fig. 5).

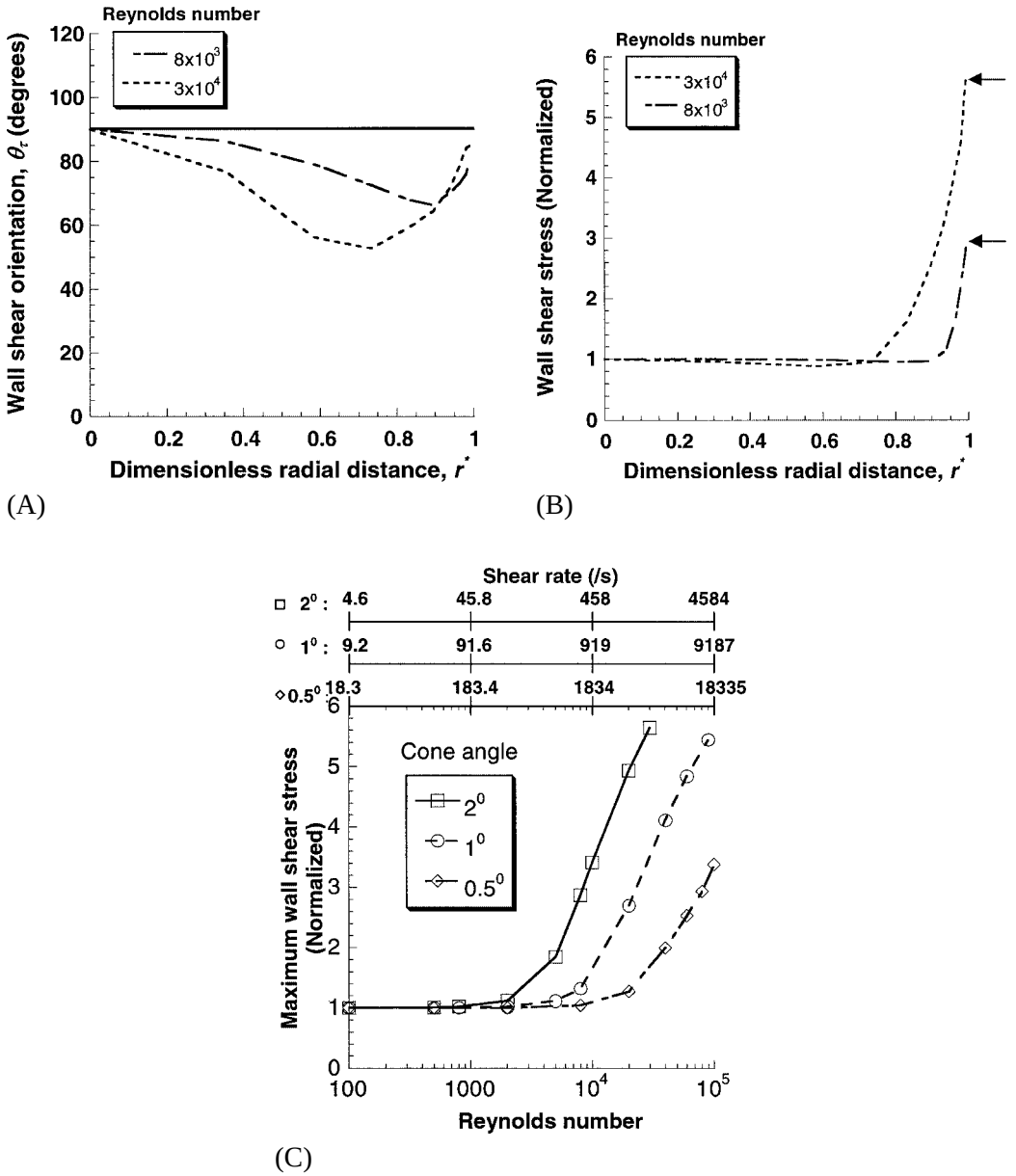

Fig. 4. Orientation and magnitude of wall shear stress at the plate surface. The numerically computed rate-of-strain tensor $\boldsymbol{S}$ was used to calculate the wall shear stress at the plate surface under primary and secondary flow conditions. (A) The orientation of the total wall shear stress τ_{tot} with respect to the radial direction for $\alpha = 2^{\circ}$. The orientation of the wall shear stress in the case of primary flow is indicated by a solid line (——) at $\theta_{\tau} = 90^{\circ}$ for all radial positions and *Re*. Broken lines depict shear stress orientation under secondary flow conditions at low *Re*($= 8 \times 10^3$, - —) and high *Re* ($= 3 \times 10^4$, - - -). (B) Variation of wall shear stress with radial position. The total shear stress under secondary flow conditions (τ_{tot}) was normalized with respect to the wall shear stress predicted by primary flow analysis. This normalized wall shear stress is plotted for low ($Re = 8 \times 10^3$) and high ($Re = 3 \times 10^4$) *Re* for a 2° cone. Arrows indicate the position of maximum wall shear stress located at the radial edge of the viscometer for both cases. (C) The maximum wall shear stress (at the radial edge) normalized with respect to primary flow is plotted as a function of *Re* and α. The shear rate corresponding to each *Re* is indicated on the top of panel C for the three different cone angles. The transformation from *Re* to shear rate is performed while assuming a fixed sample radius $R = 25$ mm.

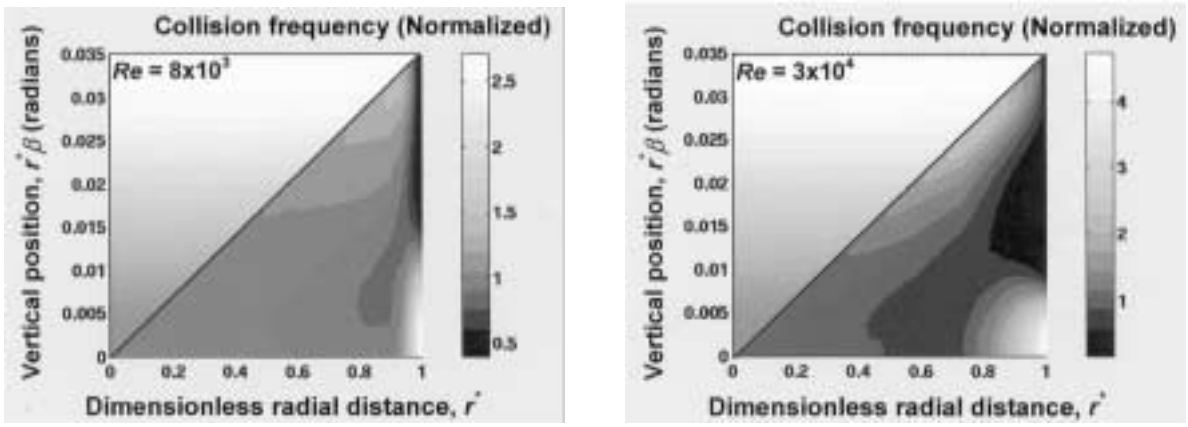

(A) (B)

Fig. 5. Inter-particle collision frequency. The local fluid velocity gradient was used to compute the collision frequency, $C(r_i^*, \beta_j)$ at the different grid points in the viscometer. The local collision frequencies were normalized with respect to the primary flow collision frequency. Panels A and B depict variation of collision frequency (normalized) with position in the viscometer with cone angle, $\alpha = 2^\circ$, for: (A) low *Re* of 8×10^3 and (B) high *Re* of 3×10^4. Here, the curvilinear grid coordinates (r^*, β) were converted to cartesian coordinates according to: X coordinate $= r^*$; Y coordinate $= r^*\beta$. Note that the positional variations illustrated here are quantitatively similar to the positional variations in inter-particle maximum normal force $F_{\max}(r_i^*, \beta_j)$ as discussed in the text.

The collision frequency at any point in the viscometer is a linear combination of the various components of the local gradient tensor (Eq. (4)). Hence, it is not surprising that the collision frequency distribution was qualitatively similar to the distribution of velocity gradients in the device. At $Re = 8 \times 10^3$ and $\alpha = 2^\circ$, there were regions in the viscometer which displayed a collision frequency that was $\sim$3 times larger than that predicted by primary flow calculations (Fig. (5A)). The effect of secondary flow on the collision frequency was most pronounced at the edge of the sample volume. Here, the normalized collision frequency varied from 2.7 near the plate surface to a value of 0.4 approximately halfway between the cone and the plate. Values significantly lesser than one were also seen close to the cone surface. The deviation of the collision frequency from primary flow predictions became more pronounced at high *Re* values (Fig. 5B). At $Re = 3 \times 10^4$ and $\alpha = 2^\circ$, the normalized collision frequency varied from 0.1 to 4.8 (Fig. 5B). The pattern of variation of the collision frequency with position was similar to that described for $Re = 8 \times 10^3$.

In spite of local variations in collision frequency, the volume-averaged collision frequency for the entire viscometer was not very different from (within 3% of) the primary flow prediction in the range of *Re* and α studied (results not shown). This behavior is similar to what is observed with the velocity gradient. Although secondary flow causes significant positional variations in the local velocity gradient, the volume-averaged value equals the primary flow shear rate. Thus, it is not surprising that the local collision frequencies, which are linear functions of the velocity gradient, also volume–average to the primary flow value. Overall, while primary flow analysis is sufficient to predict the average collision frequencies for the viscometer, detailed secondary flow analysis is necessary to quantify positional variations. Local variations in velocity gradient and collision frequency described here may influence studies of platelet and neutrophil aggregation carried out in the cone-plate viscometer.

3.5. Time-varying forces experienced by a rigid dumbbell subjected to secondary flow

During cellular aggregation the magnitude of the inter-particle normal force determines the extent to which bonds between cells are stressed. In Fig. 6, we examine the variation in inter-particle normal force with time after doublet formation for both primary (panel A) and secondary flow (panels B and C). For these calculations, the orientation of the doublet with time following collision was calculated by solving the trajectory equations for a rigid dumbbell (Eqs (21), (22)), and the normal force ($F'_{(3)}$) was calculated at each time step using Eq. (17). In all cases a shear rate of 1500/s and a cone angle of 2° was considered. The time axis in Fig. 6 was normalized with respect to the time-period of doublet rotation under primary flow conditions. This time-period is independent of position in the viscometer, and it is inversely related to the shear rate as $\sim 5\pi/G$ [4].

For primary flow (Fig. 6A), we considered two types of collisions with $\phi_1^0 = 90°$. In the first, θ_1^0 was set to 90° and in the second it was set to 45°. Both cases are hypothetical since the relative velocity between the particles is zero prior to collision. However, we choose these collisions for illustrative purposes since they maximize the doublet attachment time. The case of $\theta_1^0 = \phi_1^0 = 90°$ is also termed as a "head-on" collision. As seen in Fig. 6A, under primary flow conditions: (i) the normal force varied periodically with time, (ii) the time-period of rotation was independent of the collision orientation, and (iii) the applied force was maximum for an orbit around the vorticity axis, i.e., $\theta_1 = 90°$. It is important to note that while the normal force varies sinusoidally with orientation, force variations with time are not sinusoidal (Fig. 6A) since the rate of rotation is higher when the doublet is oriented normal to the flow and lower when it is aligned with the flow. In other words, while the force variations in Figure 6A vary periodically with time, they are not strictly sinusoidal.

For secondary flow, results at a Reynolds number of 3×10^4 and a radial distance of 0.964 are presented. In panels B and C, two different vertical positions in the viscometer are examined: $\beta = 0.0025$ radians near the plate surface, and $\beta = 0.0175$ radians midway between the cone and the plate. At $\beta = 0.0025$ radians (Fig. 6B), the time-period of force variation was reduced to 0.3 times the primary flow value and the magnitude of inter-particle force was several-fold higher than under primary flow. This is consistent with the observation of an increased gradient for the rotational velocity near the plate surface (see Fig. 3B). Also, it was seen that irrespective of the initial collision orientation ($\theta_1^0 = 90°$ or 45°), a rigid dumbbell formed following collision was pushed to a preferred orbit. This orbit was around the vorticity axis for the local flow, which approximately coincided with the plane $\theta_1 = 90°$ (results not shown, discussion follows). Figure 6C, which depicts dumbbell rotation at a vertical position halfway between the cone and the plate ($\beta = 0.0175$), illustrates a second possible scenario. In this case, secondary flow caused a decrease in the magnitude of the inter-particle force and a concomitant increase in the time-period of force variations. This is consistent with the relatively flat rotational velocity profile seen mid-way between the cone and the plate (see Fig. 3B). Irrespective of the initial collision orientation the dumbbell always aligned itself in a preferred direction such that $\mathrm{d}\theta_1/\mathrm{d}t = \mathrm{d}\phi_1/\mathrm{d}t = 0$. This suggests that the dumbbell subjected to such a velocity gradient, once it achieves its preferred orientation, may experience an infinite attachment time. With regard to whether such a scenario is possible in the cone-plate viscometer, it is important to distinguish between the simulation conditions and the real situation. In the simulation, it is assumed that the velocity gradient applied on the doublet is invariant with time. However, in a real viscometer, since the dumbbell translates in the viscometer following initial collision, the velocity gradient applied on it will vary with time. Due to this, it may be unlikely for a real doublet in the viscometer to experience infinite attachment times.

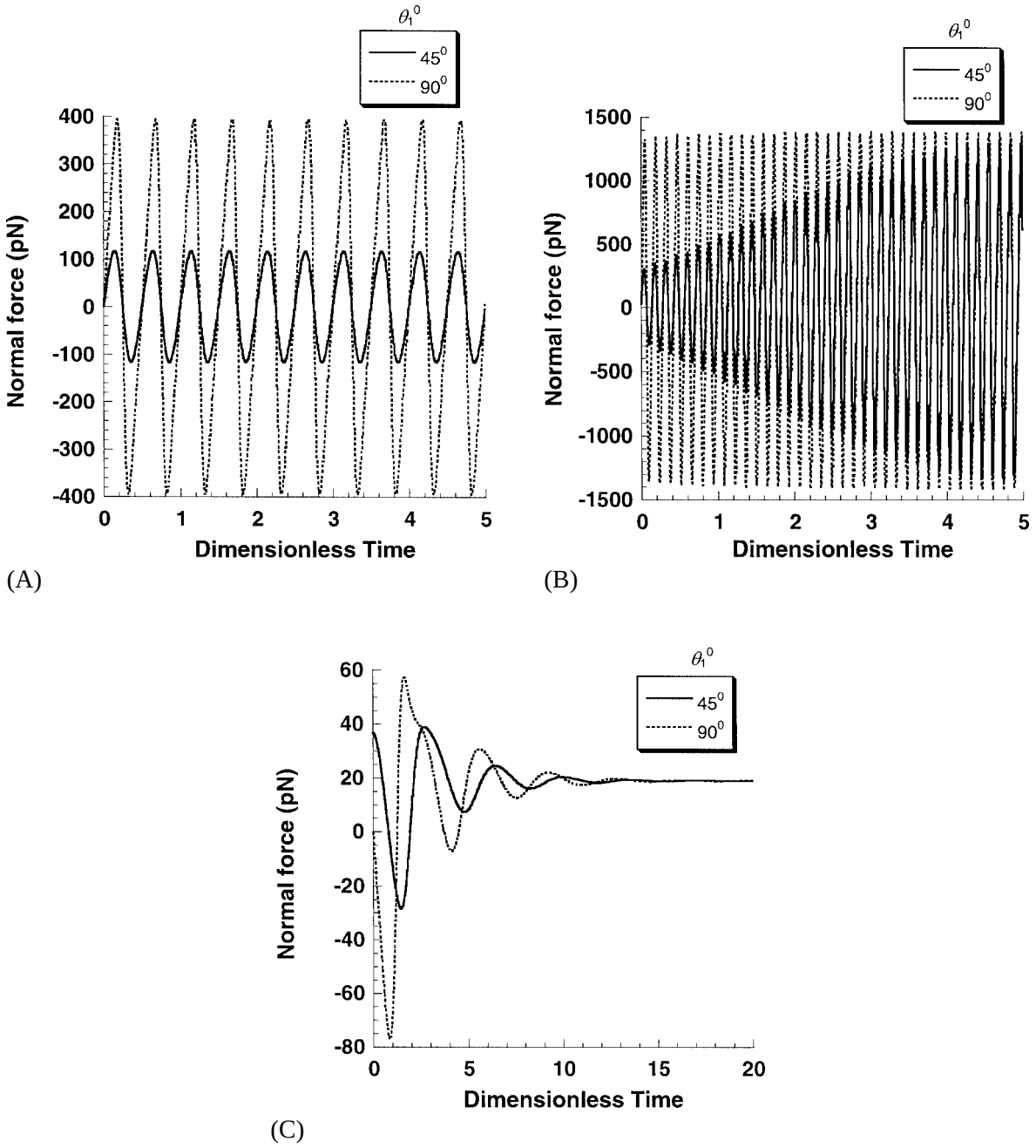

Fig. 6. Variation of inter-particle normal force with time following formation of a rigid dumbbell. Results are presented for two initial collision orientations $\theta_1^0 = 90^\circ$ and 45°($\phi_1^0 = 90^\circ$ in both cases). Cases illustrated: (A) a doublet subjected to primary flow, (B) a doublet subjected to secondary flow at $Re = 3 \times 10^4, \alpha = 2^\circ, r^* = 0.964$ (near the edge of the viscometer) and vertical position $\beta = 0.0025$ radians (near the plate surface), and (C) a doublet subjected to secondary flow at $Re = 3 \times 10^4$, $\alpha = 2^\circ, r^* = 0.964$ and $\beta = 0.0175$ radians (halfway between the cone and the plate). In all panels, time was made dimensionless with respect to the time-period of rotation of the doublet under primary flow conditions, and $t = 0$ denotes the time of doublet formation. The shear rate (G) was assumed to be 1500 s^{-1}.

Our observation that rigid dumbbells under secondary flow eventually orient themselves along a preferred direction is interesting (Figs. 6B, C). We propose here that the direction of eventual alignment depends upon the relative magnitudes of the extensional and rotational components for the flow. In relation to the cases illustrated above, primary flow (Fig. 6A) can be viewed as a special case where: (i) there are only two non-zero components of extension, both of which are orthogonal to the vorticity vector and (ii) the magnitudes of the extensional and the rotational components of the flow are equal [3]. Due to these properties, a rigid dumbbell formed following particle collision rotates in a fixed orbit. This fixed orbit, which includes the initial collision orientation, is called a Jeffery orbit [16]. In the case of secondary flow, the presence of multiple non-zero components in the velocity gradient tensor dramatically alters the magnitudes and directions of fluid extension and rotation. In particular, the local fluid flow may involve three non-zero components of extension, which in turn alter the nature of doublet rotation. In addition, under these circumstances, the flow vorticity axis may not be oriented with the vorticity axis for primary flow (X_1 or r direction). For example, in Fig. 6B, near the plate surface, in addition to two components of extension which are approximately orthogonal to the vorticity vector, there is a third small strain aligned close to the vorticity axis (data not shown). In this case, the dumbbell starting at $\theta_1^0 = 45^\circ$ re-oriented itself with respect to the vorticity axis at a rate directly related to the magnitude of the third non-zero strain (results not shown). In the second scenario in Fig. 6C, the vorticity vector and the principal-rates-of-strain are arbitrarily oriented with respect to each other. Here, it is difficult to predict the fate of the dumbbell purely by looking at the nature of the fluid flow. However as illustrated in the figure, the dumbbell eventually aligned itself in a preferred direction such that $\mathrm{d}\theta_1/\mathrm{d}t = \mathrm{d}\phi_1/\mathrm{d}t = 0$.

Overall, these results indicate that secondary flow may alter cell-cell interactions by: (i) altering the magnitude of the maximum force applied, (ii) causing changes in the time-period of force variations, and (iii) making particles experience irregular time-varying forces. It is interesting to note the dynamics that become apparent in these purely Stokesian calculations on making minor changes to the special case of an ellipsoid rotating in simple shear.

3.6. Secondary flow causes positional variations in the normal force within the viscometer

In order to assess the positional variation in inter-cellular normal force within the viscometer, we calculated for each grid point, the maximum normal force, $F_{\max}(r_i^*, \beta_j)$ experienced over the range of doublet orientations described by θ_1 and ϕ_1 (Eq. (19)). In the case of primary flow, the maximum inter-particle normal force is a linear function of shear rate G and is constant throughout the device [26]. Secondary flow however, caused positional variations in $F_{\max}(r_i^*, \beta_j)$ within the viscometer. For the cases of a 2° cone at Reynolds numbers of 8×10^3 and 3×10^4, the nature of this positional variation was quantitatively similar to the variation of the local collision frequency (Fig. 5, data not shown). Similar to Fig. 5, the deviation in the magnitude of the maximum normal force from primary flow predictions was most pronounced near the edge of the viscometer. Here, regions near the plate surface experienced significantly higher forces than regions near the cone surface. For a low *Re* of 8×10^3 and $\alpha = 2^\circ$, the ratio of the maximum force calculated by secondary flow analysis to that obtained for primary flow varied from 2.7 near the plate surface to 0.4 at a position halfway between the cone and the plate. Deviations of the maximum normal force from primary flow predictions were more pronounced for a higher *Re* of 3×10^4 at the same cone angle, where the normalized maximum normal force varied from 0.1 to 4.8. Unlike the collision frequency whose volume-averaged value for the entire viscometer did not change appreciably with *Re* and α, the collision-averaged maximum normal force $\bar{F}_{\max}$ (Eq. (20)) experienced by a doublet increased with these parameters (Table 2). On an average, a doublet suspended in a viscometer

Table 2
Collision-averaged maximum normal force, $\bar{F}_{max}$ (normalized with respect to primary flow)

Cone angle, α	$Re = 8 \times 10^3$	$Re = 3 \times 10^4$	$Re = 9 \times 10^4$
0.5°	1.00	1.00	1.03
1°	1.00	1.04	1.27
2°	1.04	1.34	not done

with a cone angle of 2° and $Re = 3 \times 10^4$, was seen to experience a force which was ∼35% higher than that predicted by primary flow analysis. Our results indicate that secondary flow causes regions of low and high normal forces within the viscometer. These regions could substantially change the local behavior of particles and the rate of particle binding in adhesion studies. We have recently described such a scenario in the context of homotypic neutrophil aggregation [23]. Such features may also affect studies of shear-induced platelet aggregation since significant secondary flow occurs at the shear rates and Reynolds numbers applied in these experiments. We are currently examining this possibility.

3.7. Particle attachment time in the viscometer varies with spatial position

The average attachment time is defined as the time spent by a newly formed doublet in the compressive force cycle following particle collision, averaged over all possible particle collision orientations. It has previously been shown that the average attachment time for simple shear is $\sim 5\pi/12G$ [5]. Therefore, for the case of primary flow, this parameter is a constant throughout the viscometer, and is inversely proportional to the shear rate G. We examined how secondary flow may affect particle attachment times. The average attachment time, t^a_{avg} was calculated for each of the $M \times N$ grid points in the viscometer (Eq. (25)). Secondary flow caused positional variations in the average attachment time in the viscometer (Fig. 7). The deviation t^a_{avg} from the primary flow value was most pronounced at the edge of the viscometer. At the lower Reynolds number of 8×10^3, the average attachment time normalized with respect to the primary flow value varied between 0.4 near the plate surface and 3.3 halfway between the cone and the plate (Fig. 7A). At $Re = 3 \times 10^4$, the normalized average attachment time varied from 0.2 to 7.6, with the minimum and the maximum values occurring at the same positions as for the low Reynolds number (Fig. 7B). The collision averaged-attachment time for the entire viscometer, $\bar{t}^a_{avg}$ was calculated using Eq. (26). In the range of *Re* and α tested $\bar{t}^a_{avg}$ did not vary by more than ±3% from the corresponding primary flow values (results not shown). Overall, these results lead us to conclude that while secondary flow does not significantly alter collision-averaged attachment times, it causes marked positional variations in local attachment times in the viscometer. The positional variations in attachment time seen here may significantly alter cell aggregation kinetics in the viscometer.

4. Conclusions

In this paper, we presented a comprehensive analysis of flow in the cone-plate viscometer as it relates to biological experiments. Dimensional analysis of the equations governing secondary flow reveal that under these conditions the velocity field is a function of two parameters: (i) the flow Reynolds number *Re* ($= R^2\Omega/\nu$) and (ii) the cone angle α. Increasing either of these parameters results in an increase in secondary flow as seen in the magnitude of the stream function, and the magnitude of the components of the velocity gradient tensor. From a practical standpoint, besides the shear rate the nature of the flow

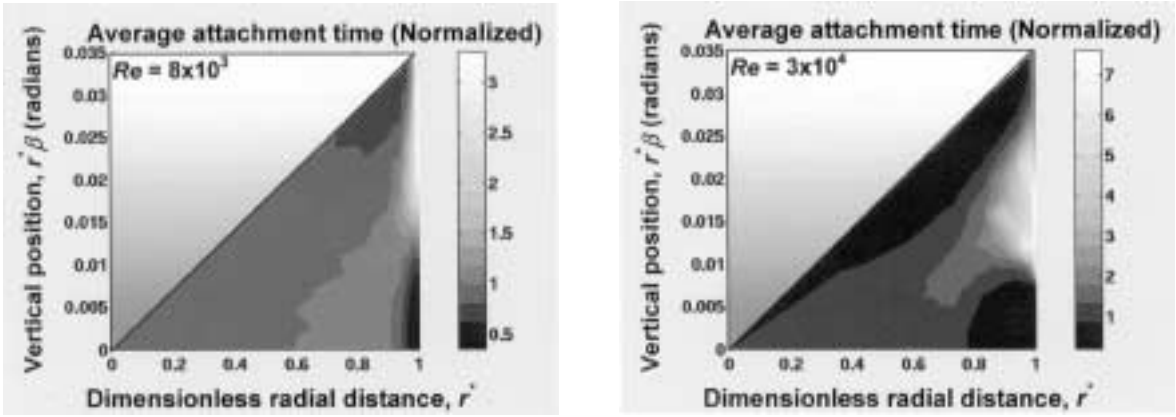

(A) (B)

Fig. 7. Average inter-particle attachment time during two-body collision. The average inter-particle attachment time is the average time spent by an interacting doublet in the compressive force zone following collision. The time spent in the compressive force zone was calculated for 1000 weighted-random initial collision orientations generated based on the collision frequency calculation, and was averaged to obtain $t^a_{\text{avg}}(r^*_i, \beta_j)$ at each position in the viscometer. This average attachment time was normalized with respect to the average attachment time predicted by primary flow analysis ($\sim 5\pi/12G$). Positional variations in average attachment time (normalized) for: (A) low *Re* (8×10^3) and (B) high *Re* (3×10^4). Here, the curvilinear grid coordinates (r^*, β) were converted to cartesian coordinates according to: X coordinate $= r^*$; Y coordinate $= r^*\beta$.

in the viscometer depends on the cone angle (α) and the volume of the sample being sheared, which controls the magnitude of the Reynolds number (*Re*). Significant secondary flow occurs at *Re* greater than $\sim$1000.

Secondary flow causes a three-dimensional flow pattern in the viscometer and results in positional variations in the wall shear stress, collision frequency, inter-particle forces and attachment times in the device. Thus, under conditions applied in biological studies, the shear stress applied on immobilized endothelial and smooth muscle cells may be several fold higher at the edge of the viscometer than that predicted by primary flow analysis. During cell–cell interactions, the interacting species may also be exposed to significantly higher (and lower) hydrodynamic forces and attachment times than under primary flow.

The probability of stable aggregate formation following collision (a quantity termed as the adhesion efficiency) is dependent on the inter-particle normal force and the attachment time. Thus, it is expected that secondary flow would cause positional variations in the adhesion efficiency. Recently we extended the analysis of flow and particle interactions in the viscometer presented in this paper to examine the effect of secondary flow on neutrophil aggregation rates in the viscometer [23]. In addition, we performed neutrophil aggregation experiments in a 2° cone-plate viscometer over a range of shear rates and sample volumes. It is satisfying to note that our theoretical predictions of neutrophil adhesion efficiencies obtained by accounting for secondary flow effects closely matches our experimentally determined values. This provides a partial validation for the results presented here.

The presence of non-linear or transient flow is inevitable in most experimental devices used in biological experiments, especially at high shear rates. It is not necessarily a liability of the cone-plate viscometer. The analysis framework described here provides a systematic methodology both to design experiments and to interpret *in vitro* data obtained from the viscometer, under these conditions. It also provides a

general scheme to model particle interactions in non-linear flow, which can be applied to other shearing devices where the flow may be complex and non-linear.

Acknowledgements

We would like to thank Dr. Johannes M. Nitsche for critical review of this manuscript, and NIH (HL63014) and The Whitaker Foundation for financial support.

Appendix A: Governing equations and boundary conditions for the flow

The governing equations for flow in a cone-plate viscometer are given below in Eqs (A.1)–(A.7) [13]. All equations are written in dimensionless form. Here, u^*, v^* and w^* are the dimensionless r, θ and ϕ components of the velocity respectively. These velocities are non-dimensionalized with respect to $R\Omega$, the rotational velocity of a point on the cone surface at the periphery of the sample being sheared. The radial distance r is normalized using R. χ^*, ζ^* and η^* are the dimensionless vorticities in the three directions, and ψ^* is the dimensionless stream function. *Re* is the flow Reynolds number, β denotes the vertical position of the fluid element, and $t^*(=t\Omega)$ is the dimensionless time.

$$\frac{\partial \zeta^*}{\partial t^*} = \frac{\partial}{\partial r^*}(\Gamma^* \chi^*) - \frac{\partial}{\partial \beta}(\Gamma^* \eta^*) - \frac{\partial}{\partial r^*}(u^* \zeta^*) + \frac{1}{r^*}\frac{\partial}{\partial \beta}(v^* \zeta^*) + \frac{1}{Re}\left[\frac{\partial^2 \zeta^*}{\partial r^{*2}} + \frac{1}{r^{*2}}\frac{\partial}{\partial \beta}\left(\frac{1}{\cos\beta}\frac{\partial}{\partial \beta}(\zeta^* \cos\beta)\right)\right], \tag{A.1}$$

$$-\zeta^* \cos\beta = E^2 \psi^*, \tag{A.2}$$

$$\frac{\partial \Gamma^*}{\partial t^*} = -u^* \frac{\partial \Gamma^*}{\partial r^*} + \frac{v^*}{r^*}\frac{\partial \Gamma^*}{\partial \beta} + \frac{1}{Re} E^2 \Gamma^*, \tag{A.3}$$

$$u^* = -\frac{1}{r^{*2}\cos\beta}\frac{\partial \psi^*}{\partial \beta}, \tag{A.4}$$

$$v^* = -\frac{1}{r^* \cos\beta}\frac{\partial \psi^*}{\partial r^*}, \tag{A.5}$$

$$\eta^* = -\frac{1}{r^{*2}\cos^2\beta}\frac{\partial \Gamma^*}{\partial r^*}, \tag{A.6}$$

$$\chi^* = -\frac{1}{r^{*2}\cos^2\beta}\frac{\partial \Gamma^*}{\partial \beta}, \tag{A.7}$$

where

$$E^2 = \frac{\partial^2}{\partial r^{*2}} + \frac{\cos\beta}{r^{*2}}\frac{\partial}{\partial \beta}\left(\frac{1}{\cos\beta}\frac{\partial}{\partial \beta}\right), \quad \zeta^* = \frac{\partial (r^* v^*)}{\partial r^*} + \frac{\partial u^*}{\partial \beta}, \quad \Gamma^* = r^* w^* \cos\beta.$$

Equation (A.1) is the ϕ component of the vorticity transport equation and Eq. (A.3) is a form of the ϕ component of the Navier–Stokes equation. These equations are written in terms of β instead of θ, since the substitution $\beta = \pi/2 - \theta$ simplifies the problem formulation [13]. At each grid point in the viscometer there are thus 7 equations and the same number of variables viz. the velocities (u^*, v^*, w^*), the vorticities $(\chi^*, \zeta^*, \eta^*)$, and the stream function (ψ^*). Γ^* is a function of w^* as depicted above. The boundary conditions for the solution are those associated with no-slip at the solid surfaces and a free surface at the edge of the viscometer. The shape of the free surface is assumed to be spherical. The boundary conditions are:

For $\beta = 0, r^* > 0$:

$$u^* = v^* = \Gamma^* = \psi^* = \frac{\partial \psi^*}{\partial r^*} = \frac{\partial \psi^*}{\partial \beta} = 0,$$

$$\zeta^* = -\frac{1}{r^{*2}} \frac{\partial^2 \psi^*}{\partial \beta^2}, \qquad \chi^* = -\frac{1}{r^{*2}} \frac{\partial \Gamma^*}{\partial \beta}, \qquad \eta^* = 0.$$

For $\beta = \alpha, r^* > 0$:

$$u^* = v^* = \psi^* = \frac{\partial \psi^*}{\partial r^*} = \frac{\partial \psi^*}{\partial \beta} = 0, \qquad \Gamma^* = r^{*2} \cos^2 \alpha,$$

$$\zeta^* = -\frac{1}{r^{*2} \cos \alpha} \frac{\partial^2 \psi^*}{\partial \beta^2}, \qquad \chi^* = -\frac{1}{r^{*2} \cos^2 \alpha} \frac{\partial \Gamma^*}{\partial \beta}, \qquad \eta^* = -\frac{2}{r^*}.$$

For $r^* = 0$:

$$u^* = v^* = \psi^* = \frac{\partial \psi^*}{\partial r^*} = \frac{\partial \psi^*}{\partial \beta} = \Gamma^* = \zeta^* = \Gamma^* \eta^* = \Gamma^* \chi^* = 0.$$

For $r^* = 1, 0 < \beta < \alpha$:

$$u^* = \psi^* = \frac{\partial \psi^*}{\partial \beta} = 0, \qquad \frac{\partial}{\partial r^*}\left(\frac{v^*}{r^*}\right) = 0, \qquad \frac{\partial}{\partial r^*}\left(\frac{\Gamma^*}{r^{*2}}\right) = 0,$$

$$\zeta^* = -\frac{1}{\cos \beta} \frac{\partial^2 \psi^*}{\partial r^{*2}}, \qquad \eta^* = -\frac{2\Gamma^*}{\cos^2 \beta}, \qquad \chi^* = -\frac{1}{\cos^2 \beta} \frac{\partial \Gamma^*}{\partial \beta}.$$

Appendix B: Derivation of equations for inter-particle forces and trajectories

Here, we describe the general methodology to compute inter-particle forces and rotational trajectories for a rigid dumbbell suspended in a fluid in motion with a known velocity gradient $\boldsymbol{G}$. The spherical coordinate system employed to calculate particle interactions is described in Fig. 8. This figure depicts the collision between two equal sized spheres of size r_P with surface roughness λ. The center to center distance between the spheres is thus $2(r_P + \lambda)$. The space-fixed coordinates (X_i) of the shear field

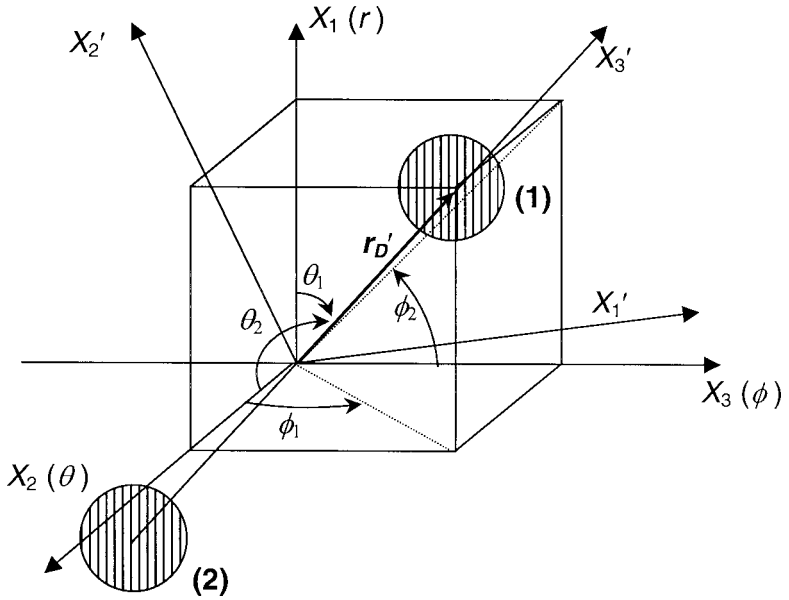

Fig. 8. Coordinate system for two-body particle hydrodynamics calculations (figure adapted from [4]). Space-fixed coordinate system is represented by X_1, X_2 and X_3. X_3 coincides with the direction of primary flow (ϕ). X_2 is the direction of the primary flow velocity gradient and it coincides locally with the viscometer's θ direction. X_1 is the vorticity axis which coincides with the viscometer radial direction, r. The origin lies at the midpoint of the line joining the centers of the two colliding spheres denoted **(1)** and **(2)**. X_i' describe the particle-fixed coordinates. X_3' lies along the line joining the centers of the two spheres. X_2' is coplanar with the X_1–X_3 plane, and X_1' is perpendicular to X_2' and X_3'. $\boldsymbol{r}_D'$ is the position vector of the center of sphere '**(1)**. (θ_1, ϕ_1) and (θ_2, ϕ_2) are polar and azimuthal angles with respect to the axes X_1 and X_2, respectively.

are depicted by X_1, X_2 and X_3. X_1 coincides with the r direction of the viscometer and corresponds to the vorticity axis for primary flow. X_2 coincides locally with the θ direction of the viscometer and corresponds to the direction of the velocity gradient for primary flow. X_3 coincides locally with the ϕ direction of the viscometer and corresponds to the direction of primary flow. The particle-fixed coordinates X_i' have origin O at the center of the doublet axis that links the two interacting spheres. X_3' lies along the doublet axis and coincides with the vector $\boldsymbol{r}_D'$ which is the position vector of the center of sphere 1, i.e., $\boldsymbol{r}_D' = (0, 0, r_P + \lambda)$. X_2' is coplanar with the $X_1 - X_3$ plane, and X_1' is perpendicular to X_2' and X_3' thus completing the orthogonal set of coordinate axes. θ_1 and ϕ_1 in the figure are polar and azimuthal angles with respect to axis X_1. θ_2 and ϕ_2 are the polar and azimuthal angles with respect to axis X_2.

The forces and torques experienced by a particle doublet subjected to creeping flow can be expressed in particle-fixed coordinates using the formulation of Brenner and O'Neill [4,9]

$$(\boldsymbol{\mathcal{F}}') = \begin{bmatrix} \boldsymbol{F}'(1) \\ \boldsymbol{F}'(2) \\ \boldsymbol{T}'(1) \\ \boldsymbol{T}'(2) \end{bmatrix} = -\mu\{(\boldsymbol{\mathcal{R}})(\boldsymbol{\mathcal{U}}') + (\boldsymbol{\Phi})(\boldsymbol{\mathcal{S}}')\}, \tag{B.1}$$

where ($\boldsymbol{\mathcal{F}}'$) is the force-torque vector for the 2 spheres, ($\boldsymbol{\mathcal{R}}$) is the grand resistance matrix, ($\boldsymbol{\Phi}$) is the shear resistance matrix, μ is the viscosity of the medium, ($\boldsymbol{\mathcal{U}}'$) is the relative velocity–spin vector, and ($\boldsymbol{\mathcal{S}}'$) = ($S'_{(11)}, S'_{(22)}, S'_{(33)}, S'_{(23)}, S'_{(13)}, S'_{(12)}$) is the shear vector of the rate of strain tensor $\boldsymbol{S}'$. $\boldsymbol{F}'(1)$ and $\boldsymbol{T}'(1)$ are the forces and torques experienced by sphere 1. $\boldsymbol{F}'(2)$, and $\boldsymbol{T}'(2)$ are the corresponding values

for sphere 2. Since the particles are of equal sizes, the spheres move with equal but opposite translational velocities, and equal rotational velocities. From symmetry, it can also be seen that the spheres experience uniform but opposite forces and equal torques, i.e., $\boldsymbol{F}'(1) = -\boldsymbol{F}'(2)$, $\boldsymbol{T}'(1) = \boldsymbol{T}'(2)$. By using these properties of symmetry, it is possible to establish the dynamics of the pair of spheres by considering sphere 1 alone. The sphere number is dropped in all the vectors and tensors that follow, since all of them refer to sphere 1.

The matrices ($\boldsymbol{\mathcal{R}}$) and ($\boldsymbol{\Phi}$) in Eq. (B.1) are independent of the nature of the flow, and are purely functions of the particle geometry. For sphere 1 these turn out to be 6x6 matrices, which can be written as [4,9]:

$$(\boldsymbol{\mathcal{R}}) = \begin{bmatrix} a & 0 & 0 & 0 & -c & 0 \\ 0 & a & 0 & c & 0 & 0 \\ 0 & 0 & b & 0 & 0 & 0 \\ 0 & c & 0 & d & 0 & 0 \\ -c & 0 & 0 & 0 & d & 0 \\ 0 & 0 & 0 & 0 & 0 & e \end{bmatrix}, \tag{B.2}$$

$$(\boldsymbol{\Phi}) = \begin{bmatrix} 0 & 0 & 0 & 0 & 2g & 0 \\ 0 & 0 & 0 & 2g & 0 & 0 \\ 0 & 0 & f+2g & 0 & 0 & 0 \\ 0 & 0 & 0 & 2h & 0 & 0 \\ 0 & 0 & 0 & 0 & -2h & 0 \\ 0 & 0 & 0 & 0 & 0 & 0 \end{bmatrix}, \tag{B.3}$$

where a, b, c, d, e, f, g, and h are force and torque coefficients for sphere 1, that are known and tabulated as functions of the sphere radius r_P and the distance between the sphere surfaces 2λ [4]. The vectors ($\boldsymbol{U}'$) and ($\boldsymbol{S}'$) in Eq. (B.1) are flow dependent quantities expressed in particle-fixed coordinates. These are evaluated based on the velocity gradient tensor $\boldsymbol{G}$ as detailed below.

The formulation of Brenner and colleagues requires us to transform the velocity gradient tensor $\boldsymbol{G}$ from space-fixed coordinates into particle-fixed coordinates. The transformation can be carried out using the relation below, written for convenience in terms of the angles (θ_2, ϕ_2).

$$\begin{pmatrix} \boldsymbol{i}_1 \\ \boldsymbol{i}_2 \\ \boldsymbol{i}_3 \end{pmatrix} = \begin{pmatrix} \cos\theta_2 \sin\phi_2 & \cos\phi_2 & \sin\theta_2 \sin\phi_2 \\ -\sin\theta_2 & 0 & \cos\theta_2 \\ \cos\theta_2 \cos\phi_2 & -\sin\phi_2 & \sin\theta_2 \cos\phi_2 \end{pmatrix} \cdot \begin{pmatrix} \boldsymbol{e}_1 \\ \boldsymbol{e}_2 \\ \boldsymbol{e}_3 \end{pmatrix}. \tag{B.4}$$

Equation (B.4) is derived based on the relative orientations of the axes X_i and X_i'. The above transformation can also be written with respect to the angles (θ_1, ϕ_1) using the following geometrical relationships:

$$\cos\theta_2 = \sin\theta_1 \cos\phi_1; \qquad \sin\theta_2 \cos\phi_2 = \sin\theta_1 \sin\phi_1; \qquad \sin\theta_2 \sin\phi_2 = \cos\theta_1. \tag{B.5}$$

In Eq. (B.4), $\boldsymbol{i}_1$, $\boldsymbol{i}_2$ and $\boldsymbol{i}_3$ are the unit vectors in space-fixed coordinates, and $\boldsymbol{e}_1$, $\boldsymbol{e}_2$ and $\boldsymbol{e}_3$ are the unit vectors in particle fixed coordinates. In standard index notation Eq. (B.4) can be written as $\boldsymbol{i}_x = L_{(xy)}\boldsymbol{e}_y$, where $\boldsymbol{L}$ is the 3×3 transformation matrix in Eq. (B.4). Here for each value of x from

1 to 3, y takes values from 1 to 3, and the repeated index y is summed over, i.e., $\boldsymbol{i}_{\mathrm{x}} = \sum_{y=1}^{3} L_{(xy)}\boldsymbol{e}_{\mathrm{y}}$. The transformation of the velocity gradient tensor into particle-fixed coordinates can then be similarly written in index notation as $G'_{(pq)} = L_{xp}L_{yq}G_{xy}$ [3]. $\boldsymbol{G}'$ is thus a function of both the position in the viscometer and the orientation of the particle doublet depicted by the angles (θ_1, ϕ_1).

Once the velocity gradient tensor $\boldsymbol{G}'$ is obtained, the rate-of-strain tensor $\boldsymbol{S}'(= 1/2(\boldsymbol{G}' + \boldsymbol{G}'^T))$ and the vorticity tensor $\boldsymbol{\Lambda}'(= 1/2(\boldsymbol{G}' - \boldsymbol{G}'^T))$ for the flow can also be calculated in particle-fixed coordinates. The shear vector $(\boldsymbol{S}')(= (S'_{(11)}, S'_{(22)}, S'_{(33)}, S'_{(23)}, S'_{(13)}, S'_{(12)})$ is then obtained from the definition involving individual elements in the rate-of-strain tensor, $\boldsymbol{S}'$.

The relative velocity-spin vector $(\boldsymbol{\mathcal{U}}')$ in Eq. (B.1) can be written for sphere 1 as

$$(\boldsymbol{\mathcal{U}}') = \begin{bmatrix} \boldsymbol{U}'_S - \boldsymbol{u}'_f \\ \boldsymbol{\Omega}'_S - \boldsymbol{\omega}'_f \end{bmatrix}, \tag{B.6}$$

where $\boldsymbol{U}'_S$ and $\boldsymbol{\Omega}'_S$ are the translational and rotational velocity vectors of sphere 1 respectively; $\boldsymbol{u}'_f$ is the undisturbed fluid velocity vector at the center of sphere 1, and $\boldsymbol{\omega}'_f$ is the undisturbed fluid vorticity vector at the center of sphere 1. $\boldsymbol{u}'_f$ and $\boldsymbol{\omega}'_f$ can be expressed as

$$\boldsymbol{u}'_f = \boldsymbol{r}'_D \cdot \boldsymbol{G}', \tag{B.7a}$$

$$\boldsymbol{\omega}'_f = -\boldsymbol{\varepsilon} : \boldsymbol{\Lambda}', \tag{B.7b}$$

where $\boldsymbol{r}'_D$ is the position vector of the sphere center and $\boldsymbol{\varepsilon}$ is the unit isotropic alternating triadic. Since the quantities in the right-hand-side of the equation are known, $\boldsymbol{u}'_f$ and $\boldsymbol{\omega}'_f$ can be evaluated.

To calculate $(\boldsymbol{\mathcal{U}}')$, we further need to evaluate the vectors $\boldsymbol{U}'_S$ and $\boldsymbol{\Omega}'_S$. This is achieved by assuming that cells interacting in suspension form a rigidly linked dumbbell upon collision [4,26]. In a rigidly linked dumbbell, the spheres cannot undergo relative rotation. Hence the components of $\boldsymbol{U}'_S$ can be written as $U'_{S(1)} = 1/2 r_D \Omega'_{S(2)}, U'_{S(2)} = -1/2 r_D \Omega'_{S(1)}$, and $U'_{S(3)} = 0$, where $r_D = 2(r_P + \lambda)$ is the size of the rigid dumbbell. Furthermore $\Omega'_{S(3)} = \omega'_{f(3)}$. Hence, for sphere 1, Eq. (B.1) can be expanded as:

$$\begin{bmatrix} F'_{(1)} \\ F'_{(2)} \\ F'_{(3)} \\ T'_{(1)} \\ T'_{(2)} \\ T'_{(3)} \end{bmatrix} = -\mu \left\{ \begin{bmatrix} a & 0 & 0 & 0 & -c & 0 \\ 0 & a & 0 & c & 0 & 0 \\ 0 & 0 & b & 0 & 0 & 0 \\ 0 & c & 0 & d & 0 & 0 \\ -c & 0 & 0 & 0 & d & 0 \\ 0 & 0 & 0 & 0 & 0 & e \end{bmatrix} \times \begin{bmatrix} \frac{1}{2}\Omega'_{S(2)} r_D - u'_{f(1)} \\ -\frac{1}{2}\Omega'_{S(1)} r_D - u'_{f(2)} \\ -u'_{f(3)} \\ \Omega'_{S(1)} - \omega'_{f(1)} \\ \Omega'_{S(2)} - \omega'_{f(2)} \\ 0 \end{bmatrix} \right.$$
$$\left. + \begin{bmatrix} 0 & 0 & 0 & 0 & 2g & 0 \\ 0 & 0 & 0 & 2g & 0 & 0 \\ 0 & 0 & f+2g & 0 & 0 & 0 \\ 0 & 0 & 0 & 2h & 0 & 0 \\ 0 & 0 & 0 & 0 & -2h & 0 \\ 0 & 0 & 0 & 0 & 0 & 0 \end{bmatrix} \times \begin{bmatrix} S'_{(11)} \\ S'_{(22)} \\ S'_{(33)} \\ S'_{(23)} \\ S'_{(13)} \\ S'_{(12)} \end{bmatrix} \right\}. \tag{B.8}$$

The unknown quantities, $\Omega'_{S(1)}$ and $\Omega'_{S(2)}$ on the right hand side of the above equation are evaluated by using the condition that a freely suspended dumbbell experiences no net torque about its center. The torque $\boldsymbol{T}'_D$ acting about the midpoint O can be written as [4]:

$$\boldsymbol{T}'_{\mathrm{D}} = \begin{bmatrix} T'_{D(1)} \\ T'_{D(2)} \\ T'_{D(3)} \end{bmatrix} = \begin{bmatrix} -r_D F'_{(2)} + 2T'_{(1)} \\ r_D F'_{(1)} + 2T'_{(2)} \\ 2T'_{(3)} \end{bmatrix}, \tag{B.9}$$

Thus, by setting $T'_{D(2)} = 0$, and $T'_{D(1)} = 0$, and substituting for the forces ($F'_{(1)}$ and $F'_{(2)}$) and torques ($T'_{(1)}$ and $T'_{(2)}$) from Eq. (B.8), we solve for $\Omega'_{S(1)}$, and $\Omega'_{S(2)}$. The dumbbell rotational velocities thus calculated can be expressed as:

$$\boldsymbol{\Omega}'_{\mathrm{S}} = \begin{bmatrix} \Omega'_{S(1)} \\ \Omega'_{S(2)} \\ \Omega'_{S(3)} \end{bmatrix} = \begin{bmatrix} \omega'_{f(1)} + \nu_D S'_{(23)} \\ \omega'_{f(2)} - \nu_D S'_{(13)} \\ \omega'_{f(3)} \end{bmatrix}, \tag{B.10}$$

where ν_D is the (flow-independent) angular velocity coefficient of a rigid dumbbell given by:

$$\nu_D = \frac{2gr_D - 4h - (r_D)^2 a/2 + cr_D}{(r_D)^2 a/2 - 2r_D c + 2d}. \tag{B.11}$$

The inter-particle force is then calculated by substituting $\boldsymbol{\Omega}'_S$ from Eq. (B.10) into Eq. (B.8). It can be shown through simple algebraic manipulations that the equations for the components of the inter-particle force reduce to:

$$F'_{(1)} = -\mu\left(\left(-\frac{1}{2}ar_D\nu_D + c\nu_D + 2g\right)S'_{(13)} + a\left(\frac{1}{2}r_D\omega'_{f(2)} - u'_{f(1)}\right)\right), \tag{B.12}$$

$$F'_{(2)} = -\mu\left(\left(-\frac{1}{2}ar_D\nu_D + c\nu_D + 2g\right)S'_{(23)} + a\left(-\frac{1}{2}r_D\omega'_{f(1)} - u'_{f(2)}\right)\right), \tag{B.13}$$

$$F'_{(3)} = -\mu((f + 2g)S'_{(33)} - bu'_{f(3)}). \tag{B.14}$$

Here, $F'_{(1)}$ and $F'_{(2)}$ are shear force components acting along the X'_1 and X'_2 axes respectively, while $F'_{(3)}$ is the normal force acting along the line joining the centers of the interacting spheres. Substituting for the components of the rate-of-strain tensor, the velocity and the vorticity vectors for the fluid in Eqs (B.12)-(B.14) above, and using the trigonometric relations in Eq. (B.5), allows us to express the force in terms of the dumbbell orientation (θ_1, ϕ_1) and the velocity gradient tensor $\boldsymbol{G}$ in space-fixed coordinates. It can be shown that the expression for the inter-particle normal force then reduces to the one in Eq. (17).

To calculate the rotational trajectory of doublets formed following particle collision, the angular velocity vector $\boldsymbol{\Omega}'_S$ (Eq. (B.10)) is transformed into space-fixed coordinates using Eq. (B.4). This transformation can be written in index notation as:

$$\Omega_{S(x)} = L_{(xy)}\Omega'_{S(y)}, \tag{B.15}$$

where $\mathbf{\Omega}_S$ is the angular velocity vector in space-fixed coordinates, and $\boldsymbol{L}$ is the 3×3 matrix in Eq. B4. The contributions of the components $\mathbf{\Omega}_S$ to the rates of change of the polar and azimuthal angles are then determined to obtain the trajectory equations for the rigid dumbbell. These equations are obtained by coordinate geometry manipulations similar to those described by Jefferey [16] and can be written as:

$$\frac{\mathrm{d}\theta_1}{\mathrm{d}t} = \Omega_{S(3)} \cos\phi_1 - \Omega_{S(2)} \sin\phi_1, \tag{B.16}$$

$$\frac{\mathrm{d}\phi_1}{\mathrm{d}t} = \Omega_{S(1)} - \frac{\cos\theta_1}{\sin\theta_1}\left[\cos\phi_1 \Omega_{S(2)} + \sin\phi_1 \Omega_{S(3)}\right]. \tag{B.17}$$

These equations describe the change in doublet orientation with respect to the vorticity axis, X_1, with time following inter-particle collision. Again, by expressing the fluid flow quantities in terms of the velocity gradient tensor and using the trigonometric relations in Eq. (B.5), it can be shown that Eqs (B.16) and (B.17) reduce to the form expressed in Eqs (21) and (22) in the text.

References

[1] C.K. Aidun, Y. Lu and E.J. Ding, Direct analysis of particulate suspensions with inertia using the discrete Boltzmann equation, *J. Fluid Mech.* **373** (1998), 287–311.
[2] H. Akima, A new method of interpolation and smooth curve fitting based on local procedures, *J. ACM* **17** (1970), 589–602.
[3] R. Aris, *Vectors, Tensors and the Basic Equations of Fluid Mechanics*, Dover Publications, Inc., New York, 1989.
[4] P.A. Arp and S.G. Mason, The kinetics of flowing dispersions VIII. Doublets of rigid spheres (Theoretical), *J. Colloid Interf. Sci.* **61** (1977), 21–43.
[5] P.A. Arp and S.G. Mason, Orthokinetic collisions of hard spheres in simple shear flow, *Can. J. Chem. Eng.* **54** (1976), 3769–3774.
[6] G.I. Bell, Estimate of the sticking probability for cells in uniform shear flow with adhesion caused by specific bonds, *Cell Biophys.* **3** (1981), 289–304.
[7] B.R. Bird, W.E. Stewart and E.N. Lightfoot, *Transport Phenomena*, John Wiley & Sons, New York, 1994.
[8] K.E. Brenan, S.L. Campbell and L.R. Petzold, *Numerical Solutions of Initial Value Problems in Differential-Algebraic Equations*, Elsevier Science Publ. Co., 1989.
[9] H. Brenner and M.E. O'Neill, On the Stokes resistance of multiparticle systems in a linear shear field, *Chem. Eng. Sci.* **27** (1972), 1421–1439.
[10] C.F. Dewey, Effects of fluid flow on living vascular cells, *J. Biomech. Eng.* **106** (1984), 31–35.
[11] C.W. Evans and J. Proctor, A collision analysis of lymphoid cell aggregation, *J. Cell Sci.* **33** (1978), 17–36.
[12] M.E. Fewell, The secondary flow of Newtonian fluids in cone-and-plate viscometers, Ph.D. Dissertation, Rice University, 1974.
[13] M.E. Fewell and J.D. Hellums, The secondary flow of Newtonian fluids in cone-and-plate viscometers, *Trans. Soc. Rheol.* **21** (1977), 535–565.
[14] S. Goto, Y. Ikeda, E. Saldivar and Z.M. Ruggeri, Distinct mechanisms of platelet aggregation as a consequence of different shearing flow conditions, *J. Clin. Invest.* **101** (1998), 479–486.
[15] P.Y. Huang and J.D. Hellums, Aggregation and disaggregation kinetics of human blood platelets: Part I. Development and validation of a population balance method, *Biophys. J.* **65** (1993), 334–343.
[16] G.B. Jeffery, The motion of ellipsoidal particles immersed in a viscous fluid, *Proc. R. Soc. (Lond.)* **A102** (1922), 162–179.
[17] A. Karnis, H.L. Goldsmith and S.G. Mason, The flow of suspensions through tubes V. Inertial effects, *Can. J. Chem. Eng.* **44** (1966), 181–193.
[18] S. Neelamegham, A.D. Taylor, J.D. Hellums, M. Dembo, C.W. Smith and S.I. Simon, Modeling the reversible kinetics of neutrophil aggregation under hydrodynamic shear, *Biophys. J.* **72** (1997), 1527–1540.
[19] S. Neelamegham, A.D. Taylor, H. Shankaran, C.W. Smith and S.I. Simon, Shear and time dependent changes in Mac-1, LFA-1, and ICAM-3 binding regulate neutrophil homotypic adhesion, *J. Immunol.* **164** (2000), 3798–3805.
[20] M. Ohno, G.H. Gibbons, V.J. Dzau and J.P. Cooke, Molecular and cellular biology: Shear stress elevates endothelial cGMP: Role of a potassium channel and G protein coupling, *Circulation* **88** (1993), 193–197.
[21] J.G. Savins and A.B. Metzner, Radial (secondary) flows in rheogoniometric devices, *Rheologica Acta* **9** (1970), 365–373.

[22] H.P. Sdougos, S.R. Bussolari and C.F. Dewey, Secondary flow and turbulence in a cone-and-plate device, *J. Fluid Mech.* **138** (1984), 379–404.
[23] H. Shankaran and S. Neelamegham, Non-linear flow affects hydrodynamic forces and neutrophil adhesion rates in cone-plate viscometers, *Biophys. J.* **80** (2001), 2631–2648.
[24] M.V. Smoluchowski, Versuch einer mathematischen theorie der koagulationskinetik kolloider losungen, *Zeitschrift Phys. Chem.* **92** (1917), 129–168.
[25] A.D. Taylor, S. Neelamegham, J.D. Hellums, C.W. Smith and S.I. Simon, Molecular dynamics of the transition from L-selectin- to β_2-integrin-dependent neutrophil adhesion under defined hydrodynamic shear, *Biophys. J.* **71** (1996), 3488–3500.
[26] S.P. Tha and H.L. Goldsmith, Interaction forces between red cells agglutinated by antibody I. Theoretical, *Biophys. J.* **50** (1986), 1109–1116.
[27] S.P. Tha, J. Shuster and H.L. Goldsmith, Interaction forces between red cells agglutinated by antibody II. Measurement of hydrodynamic force of breakup, *Biophys. J.* **50** (1986), 1117–1126.
[28] P.S. Tsao, R. Buitrago, J.R. Chan and J.P. Cooke, Fluid flow inhibits endothelial adhesiveness nitric oxide and transcriptional regulation of VCAM-1, *Circulation* **94** (1996), 1682–1689.
[29] R.M. Turian, Perturbation solution of the steady Newtonian flow in the cone and plate and parallel plate systems, *Ind. Eng. Chem. Fundam.* **11** (1972), 361–368.
[30] C.T. Wagner, W. Durante, N. Christodoulides, J.D. Hellums and A.I. Schafer, Hemodynamic forces induce the expression of heme oxygenase in cultured vascular smooth muscle cells, *J. Clin. Invest.* **100** (1997), 589–596.